ADVANCED FUNCTIONAL MATERIALS
www.afm-journal.de

Advances in Optical Imaging and Optical Communications Based on High-Quality Halide Perovskite Photodetectors

Daming Zheng and Thierry Pauporté**

Metal halide perovskites are widely used in the preparation of photodetectors (PDs) due to their excellent photoelectric properties, tunable band gap, low cost, and rapid processing in solutions. Although 3D perovskite PDs exhibit exceptional performance, their practical applications are limited due to instability issues. Conversely, 2D perovskite PDs are gaining popularity due to their superior environmental stability. To produce efficient and stable perovskite-based PDs, it is crucial to control the film formation process to achieve high-quality perovskite films. This paper examines the impacts of perovskite film preparation process and crystallinity on the photoelectric properties of PDs and presents important observations regarding the crystallization and phase dynamics that occur during perovskite film formation. These insights have practical implications on the design and preparation of high-performance and stable metal halide perovskite photodetectors, particularly in the domains of optical communications and imaging. They offer valuable guidance for next researchers and developers seeking to improve the functionality and marketability of photodetectors using perovskite films.

1. Introduction to Photodetectors and Halide Perovskites

In recent years, with the fast development of the Internet of Things and artificial intelligence technology, the entire information technology industry has gradually entered the era of optical information. Specifically, photodetectors (PDs), which convert optical signals into electrical signals, facilitate the initial acquisition of information. They have a wide range of applications, in various fields, such as biological detection, medicine, optical imaging, optical communication, and military domains.[1–4] PDs based on semiconductors typically use electrical junctions that convert photons into charge. The absorbed photons of energy superior to the semiconductor bandgap cause valence band electrons to move into the conduction band, leaving behind holes in the valence band. These photogenerated charge carriers can be collected under the influence of an intrinsic or external applied electric field.

The current trend in the development of information technology is toward high-performance miniaturized devices. This is a crucial step toward faster, high-density integration and lower power consumption of photonic technologies, such as optical computing, artificial intelligence, high-sensitivity detection, on-chip quantum information, etc.[5–8] To achieve optimal performance, the active layer in photodetectors (PDs) must possess several key characteristics. These include a high absorption coefficient, which allows full light absorption and renders possible the reduction of the absorbing layer thickness and their integration in flexible devices. Additionally, high carrier mobility is necessary, as it determines the overall movement of electrons and holes in PDs. Lastly, efficient carrier collection is crucial for the overall collection of electrons and holes in PDs. PDs are typically designed with either vertical or lateral structures, depending on the spatial arrangement of the photoactive medium and electrodes. Vertical PDs (**Figure 1**a) have a small electrode spacing and short carrier transit length, which, when combined with interfacial layers, effectively reduces dark current under reverse bias, resulting in high detectivity. On the other hand, lateral PDs have a simple device structure consisting of a photoactive layer and either two parallel electrodes (Figure 1b) or three metal electrodes (source, drain, and gate), making them easier to fabricate (Figure 1c). Currently most commercialized PDs are based on inorganic semiconductor materials such as silicon (Si). However, their fabrication process as large-area and flexible PDs is complex and costly, which hinders their further development.[9–12]

As photodetectors (PDs) play a fundamental role in optical imaging and optical communications devices, it is important to accurately evaluate their performances and quality. The main parameters for this include:

D. Zheng, T. Pauporté
Chimie ParisTech
PSL Research University
CNRS
Institut de Recherche de Chimie Paris (IRCP)
UMR8247, 11 rue P. et M. Curie, Paris F-75005, France
E-mail: daming.zheng@chimieparistech.psl.eu;
thierry.pauporte@chimieparistech.psl.eu

The ORCID identification number(s) for the author(s) of this article can be found under https://doi.org/10.1002/adfm.202311205

DOI: 10.1002/adfm.202311205

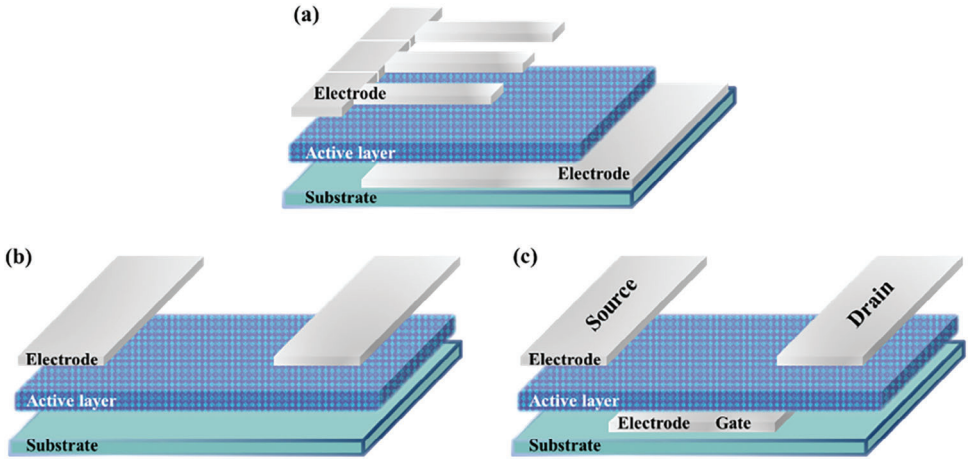

Figure 1. Schematic structures of a) a vertical PD, b) a lateral PDs with two parallel electrodes, and c) a lateral PDs with three metal electrodes (source, drain, and gate).

$$\text{The spectral responsivity}: \ R = \frac{I_\lambda}{P_\lambda} = \frac{\text{EQE}\,(\%)\,\lambda q}{hc} \tag{1}$$

where I_λ is the photogenerated current and P_λ is the incident optical power at the radiation wavelength λ. R is related to the external quantum efficiency (EQE), the elemental charge (q), the Planck constant (h), and the light velocity (c).

$$\text{The on} - \text{off ratio}: \ \text{on/off} = \frac{I_\text{p}}{I_\text{d}} \tag{2}$$

which represents the ratio of the photocurrent (I_p) to the dark current (I_d). In general, the lower I_d, the higher the I_p, and the better the performance of the PDs.

The response time (τ) indicates the speed of response to incident light. One distinguish the rise time (τ_rise) and decay time (τ_decay). τ_rise refers to the time it takes for the photocurrent to increase from 10% to 90% of its maximum value after light on. τ_decay refers to the time it takes for the photocurrent to decrease from 90% to 10% of its maximum value when incident light switched off.

$$\text{Detectivity}: \ D^* = R\sqrt{A\Delta f}/I_\text{n} \tag{3}$$

where I_n is the noise current, Δf is the bandwidth which defines the range of frequencies a system can accommodate, and A is the area of PDs. This parameter represents the detection capability of a PD. The stronger D^*, the better performance of the PD.

The linear dynamic range (LDR), represented in dB, describes the range within which the detector output scales linearly with the input irradiance. LDR is calculated as:

$$\text{LDR} = 20\log\frac{J_\text{upper}}{J_\text{lower}} = 20\log\frac{L_\text{upper}}{L_\text{lower}} \tag{4}$$

where J stands for the photocurrent density in A cm^{-2} and L denotes the light intensity in W cm^{-2}.

In the context of a fixed detection area, the resolution of an image sensor is typically determined by the number of pixels it has. Generally, a higher number of pixels results in higher resolution and better image quality.

With time, a variety of new nanomaterials have been developed and used in a wide range of photoelectric devices.[12–14] Among them, 3D metal-lead halide perovskite semiconductors have become potential candidates for multifunctional light absorbing material and next-generation light sensors in the field of optoelectronic devices. Halide perovskites have the ABX_3 chemical formula where B is a divalent metal cation (B site; e.g., Sn^{2+} and Pb^{2+}) which is coordinated to six halide anions (X site; e.g., I^-, Br^-, and Cl^-) forming a BX_6 octahedral framework. The center of four BX_6^{4-} octahedra defines the A-site that is occupied by a monovalent cation (e.g., MA^+, FA^+, and Cs^+). $CH_3NH_3PbX_3$ is the most popular perovskite family which was applied to solar cells by the Miyasaka group. Rapid progresses have risen the power conversion efficiency of perovskite solar cells up to a present 26.1% record within just over fourteen years.[15–17] This efficiency is now comparable to that of commercial silicon-based cells. Halide perovskite compounds exhibit a high charge carrier mobility, excellent absorption coefficient, tunable band gap (luminescence covers the entire visible range), low preparation cost, broad material sources, and easy large-scale production, offering wide applications in the field of optoelectronic devices.[18–23]

Although the conversion efficiency of 3D perovskite optoelectronic devices has improved significantly, their stability is still rather poor and the structure can be easily destroyed under environmental conditions.[23–32] These are considered as a stumbling block for their potential commercialization. With the development and optimization of various types of perovskites, the exceptional adjustability and thermal stability of the developed metal halide perovskites with a 2D layered structure have garnered significant attention in the field of photoelectric research. 2D perovskites are represented by the formula $(A')_m(A)_{n-1}B_nX_{3n+1}$.[33–35] This formula includes divalent (m = 1) or monovalent (m = 2) spacer cations that connect the inorganic $(A)_{n-1}B_nX_{3n+1}$ 2D sheets, forming a bilayer or monolayer. The layer thickness of the metal halide sheets can be adjusted by tuning the

precursor composition, with n indicating the layer thickness. The organic A′-site cation can be arbitrarily long, allowing for the use of large, high-aspect-ratio cations such as aliphatic- or aromatic-based compounds. It is worth noting that $n = i$ (infinite) corresponds to the 3D perovskite, whereas $n = 1$ represents the pure 2D, and $2 \leq n \leq 5$ is often referred to as quasi-2D. For $n > 5$, we refer to as quasi-3D perovskites. Additionally, a mixture of 3D perovskite and low-n phases (e.g., $n \leq 3$) can form even when n values are high. As n increases, the differences in thermodynamic stability in the high-n structures become smaller, making it difficult to prepare phase-pure high-n structures. Thus, the n value of such perovskites is usually described based on the precursor composition. Introducing suitable low dimensional structures can significantly enhance the structural robustness of perovskite materials, thereby offering an efficient approach to bolster the stability of devices. Reducing the dimensionality of perovskite materials can significantly change the properties of the excitons inside the materials to exhibit different photoelectric properties, which has great application potential in PDs field.[35–38]

Nevertheless, it is crucial to highlight that although shielding 3D perovskite against moisture infiltration through the integration of substantial organic cations is paramount, the incorporation of such sizable organic cations in 2D perovskite will indubitably hinder the device's efficiency due to the constraining presence of insulating spacer cations, which can impede the transport of charge carriers.[39–41] Because the polycrystalline nature of perovskite films, there are also inevitable structural defects and grain boundary defects in perovskite films. It results in poor charge transport capacity and reduced carrier mobility.[42,43] In addition, the film treated with the solution process is not dense, crystallizes poorly, and the nucleation of crystallization is difficult to control, leading to deterioration of the photoelectric performance of the devices.[44,45] Therefore, perovskite PDs with good performance are rarely found in applications, especially in optical imaging and optical communications.

Recently, there have been several reviews on perovskite-based photodetectors (PDs).[46–54] However, these reviews primarily focus on presenting the most recent advances in perovskite-based PDs, for example, introducing the progress of different types and different wavelength selectivity of perovskite-based PDs, with little attention paid to the effects of perovskite film quality and crystallinity on the performance of PDs. Since this is the most important layer in various PD-based devices, more attention must be paid to it.

The present paper systematically investigates the crystallization kinetics and film formation processes of 3D to 2D perovskites for photodetectors (PDs). First, we introduce the recent research progresses in 3D to 2D halide perovskite PDs for optical communication and imaging. Subsequently, we provide a fundamental understanding of 3D to 2D perovskite films integrated in PDs. Next, we review various strategies adopted to improve perovskite PDs, including component engineering, interface engineering, heterojunction engineering, and film crystallinity engineering. Finally, based on the historical and current research status of perovskite PDs, we propose a set of challenges and solutions to advance the future development of perovskite PDs, aiming to achieve remarkable performance, rapid response time, and unparalleled environmental stability.

2. Application of Perovskite PDs

Recently, the rapid development of perovskite solar cells and their superior photoelectric performance have significantly improved the photoelectric conversion efficiency.[16,17] This progress has also laid the foundation for the exploration of high-performance perovskite PDs. As an optical sensor widely used in biomedical imaging, consumer electronics, and military applications, with the rapid increase in demand for advanced image sensing and optical communication technology, the need for sensitive and fast response PDs is also increasing.[19,55,56] As the application of perovskite semiconductor materials has been well-developed in the field of optoelectronics, the performance indicators of perovskite PDs have reached a very high level comparable to that of commercial PDs,[12] so these devices have the potential to be extensively utilized in optical communications and image sensing applications.

2.1. Perovskite PDs for Optical Communication

PDs are crucial in optical communication systems as they enable efficient optoelectronic signal conversion. The speed at which PDs respond is crucial in determining the overall bandwidth of the system.[57,58] Most present-day commercial photodetectors (PDs) rely on conventional inorganic semiconductors, namely silicon (Si) and indium gallium arsenide (In/Ga/As), that necessitate costly high-vacuum fabrication methods.[9,11] However, metal halide perovskite, a novel and cost-effective semiconductor, that can be prepared from solutions, exhibits excellent light absorption and high carrier mobility. Consequently, it has garnered significant attention in the field of photoelectric detection applications, leading to extensive research efforts.[2,18,40]

In order to achieve fast response and reliable optical signal transmission of perovskite-based PDs, lots of researchers have put great efforts into the controllable synthesis and performance optimization of the materials. For example, Bao et al. have shown that the device fabricated from the inorganic 3D perovskite $CsPbIBr_3$ exhibits a detection limit of approximately 21.5 pW cm^{-2} and a rapid response time of 20 ns. (**Figure 2**a,b). The perovskite PDs were successfully integrated into an optical communication system and their application as an optical signal receiver for the transmission of text and audio signals was demonstrated.[55] Liu et al. suggested a method of P-type doping for 3D $MAPbI_3$ perovskite films using Cu ions. This approach aimed to enhance the crystallinity and photoelectric performance of the self-powered hole conductor-free perovskite PDs (Figure 2c,d). The device achieved an ultimate photoreaction rate of approximately 5 µs. The successful integration of perovskite PDs into an optical communication system enabled accurate character transmission and high fidelity of audio signals in an optical signal receiver for digital signal transmission.[59]

Moreover, Kang et al. reported a hybrid silicon-based light detection by combining $CsPbBr_3$ perovskite nanocrystals (NCs) with a light attenuation time of 4.5 ns, which can be used in the ultraviolet to visible light conversion layer for fast UV optical communication with solar iris (Figure 2e,f).[60] To enhance the accuracy and efficiency of signal detection and decoding, Huang et al. introduced dual-band PDs as a viable solution for receiver terminals in visible light communication. Using $MAPbBr_3$ and

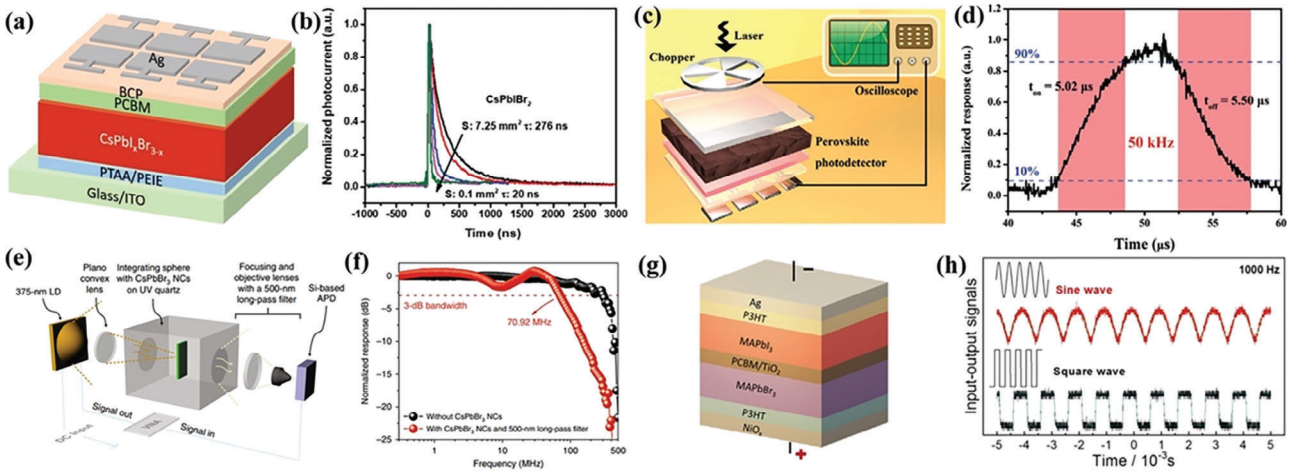

Figure 2. a) Schematic structure of PDs based on CsPbI$_x$Br$_{3-x}$ perovskite. b) The photocurrent with different active areas of PDs based on CsPb(IBr$_2$). a,b) Reproduced with permission.[55] Copyright 2018, Wiley-VCH. c) Schematic illustration to measure the photoresponse speed of the perovskite PDs. d) A single photoresponse curve at 50 kHz. c,d) Reproduced with permission.[59] Copyright 2022, Wiley-VCH. e) Schematic illustration of a small-signal frequency response measuring device using laser diode. f) The normalized frequency response of a laser diode and avalanche photodiode without CsPbBr$_3$ perovskite nanocrystals, and a with CsPbBr$_3$ perovskite nanocrystals and 500-nm long-pass filter. e,f) Reproduced with permission.[60] Copyright 2019, Springer. g) Schematic structure of dual-band PDs. h) Temporal response of device to sine wave and square wave signals. g,h) Reproduced with permission.[56] Copyright 2020, American Chemical Society.

MAPbI$_3$ as photosensitive layers, the device could detect signals from commercial white light-emitting diodes (LED) at two different wavelengths by pile up two photodiodes with opposite polarity, with switching rates approaching 1000 Hz (Figure 2g,h). This characteristic guaranteed its effectiveness as a proficient data receiver.[56] In addition to 3D perovskite PDs that integrate well with optical communication devices, 2D/quasi-2D perovskite also shows great potential in optical communication by enhancing film quality and optimizing performance. It is worth mentioning that for photodetectors based on 2D/quasi-2D perovskite, the orientation of the quantum well of the perovskite itself has a great impact on the preparation of photodetectors with different structures: the orientation of quantum wells of a 2D/quasi-2D perovskite must be preferably aligned perpendicular to the substrate for vertical PDs (Figure 1a), while it must be parallel to the structure in lateral PDs (Figure 1b,c) (see section 3.2).

Wang et al. have reported on a strategy to use formamidinium chloride (FACl) as an additive to create quasi-2D perovskite films that exhibit high quality, crystallinity, and exceptional environmental stability. Subsequently, localized surface plasmonic resonances (LSPRs) have been achieved through the incorporation of metal nanostructures (Au/Ag) onto the substrate. This integration has significantly enhanced the optical response performance of the device, resulting in an impressive ultimate response speed of 9 μs.[61] In addition, the device demonstrated exceptional stability in various environmental conditions. Finally, it was successfully integrated and tested in an optical communication system. The results indicate that with appropriate material synthesis methods, improvement of film crystallinity and optimization of device structure, a window for high-performance metal halide perovskite PDs is opened, and efficient optical detection is realized in an advanced integrated optical communication system.

2.2. Perovskite PDs for Image Sensing

At present, the imaging devices are digital cameras, whose main components are a charge-coupled device (CCD) or a complementary metal oxide semiconductor (CMOS), manufactured by relatively complex techniques.[62,63] After continuous development, the limitations of silicon have almost reached their bottleneck when it comes to Si-CCD and Si-CMOS. However, there is hope on the horizon with a new generation of semiconductor perovskite materials that are available to fill the gaps in current technology. These materials offer a diverse family of options with tunable intrinsic properties. They are also easy to fabricate using solution processes and have good ductility, making them highly competitive for future smart applications such as photoelectric sensing and imaging.[19,64,65] In order to expand the range of applications for perovskite photodetectors (PDs), researchers have utilized various methods to fabricate PDs with higher resolution. This is because resolution is a crucial parameter in imaging with PDs units. Achieving higher resolution requires more pixels, which must be smaller in size. The solution method for producing perovskite materials simplifies the manufacturing process of PDs units, allowing for the fabrication of individual perovskite PDs units in smaller sizes through a flexible process. Based on this understanding, Wu et al. reported an ultrathin perovskite PDs array with ultralight weight and excellent flexibility.[64] The active layer of the patterned inorganic perovskite CsPbBr$_3$ films was prepared using a vacuum-assisted drop-casting method, resulting in precise pixel positioning, controllable morphology, and uniform film size. As shown in **Figure 3**b,c, hemispherical supported ultrathin flexible PD arrays realize light distribution imaging and have potential application in retinal visual perception. Jang et al. reported a simple method for transferring the perovskite pattern to the planar or nonplanar surface using a mobile polymer.[23] The excellent adhesion between the film and the

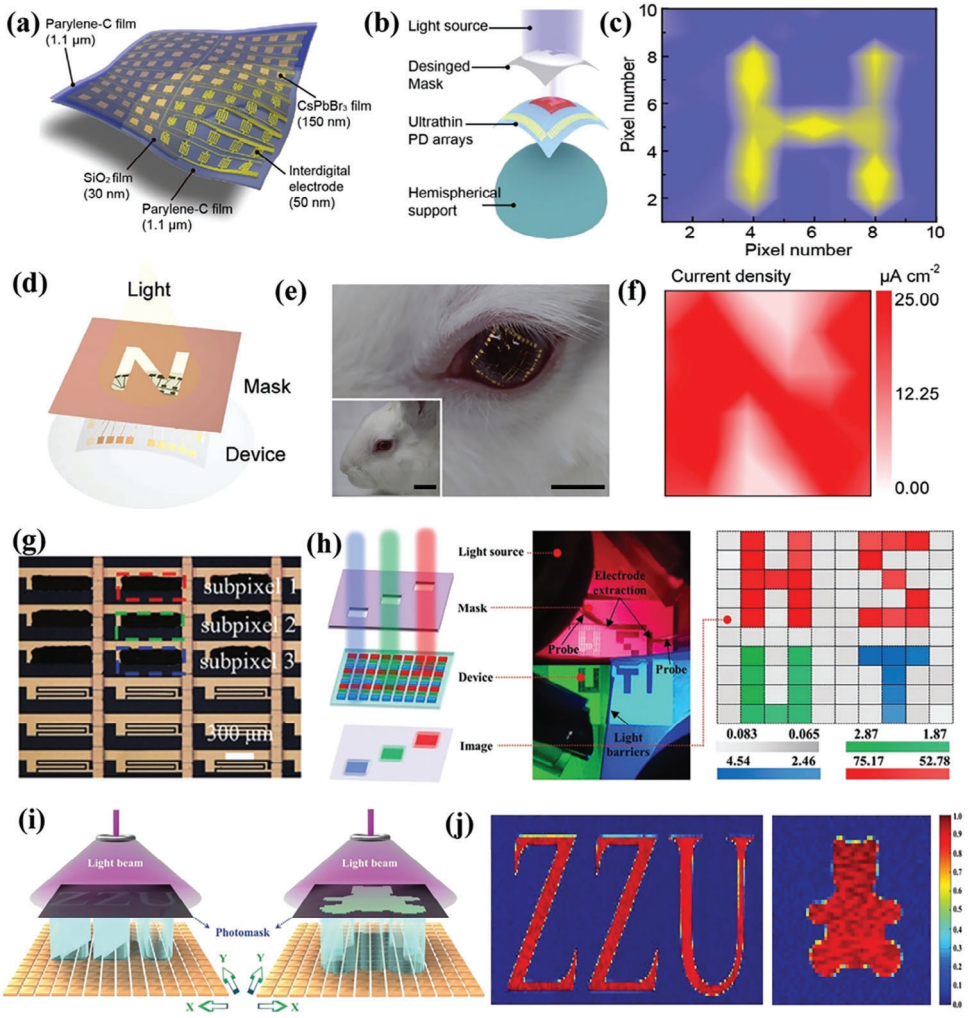

Figure 3. a) Schematic diagram of the ultrathin perovskite device. b) Schematic diagram of a measuring device that mimics the human eye. c) PD arrays lamination of light intensity distribution imaging results with hemispherical support and H-shaped. a–c) Reproduced with permission.[64] Copyright 2021, Wiley-VCH. d) Schematic diagram of the device measuring light incident on a designated area. e) Photograph is a white rabbit wearing an artificial intelligence contact lens. Scale bar: 1 cm. f) The resulting image is mapped by smart contact lens. d–f) Reproduced with permission.[23] Copyright 2021, Wiley-VCH. g) Photographs of perovskite image photodetector on a glass substrate. h) The schematic diagram and equipment photograph of the image photodetector array used for detecting light distribution, as well as the normalized current mapping results of the full-color image photodetector after image illumination using a shadow mask. The numerical units are nA. g,h) Reproduced with permission.[66] Copyright 2021, Wiley-VCH. i) Mechanism of the device imaging process. j) The imaging results are the emblem of Zhengzhou University "ZZU" and the symbol of a bear. i,j) Reproduced with permission.[67] Copyright 2019, Wiley-VCH.

target surface enabled the device to be conveniently positioned on various substrates through sacrificial film removal. Through employing this transfer technique, a photo-sensing array using perovskite can be fabricated onto soft contact lenses, as proven by in vivo experiments conducted on rabbits, thereby showcasing its durability against wear and tear (Figure 3e,f). Wang et al. utilized the high-resolution electro-fluidic dynamic pressure method to fabricate pixelated perovskite photodetectors (PDs) with full-color distribution. Notably, they employed the ionic liquid methylammonium acetate as a solvent for this purpose.[66] The photoconductor structure of the PDs device is represented by the overall diagram and structure of the 10 × 10 pixel (10 × 10 × 3 sub-pixel) device in Figure 3g. The electrofluid dynamics method used in the fabrication process resulted in PDs unit arrays with excellent imaging performance, as demonstrated by the clear imaging of the letter diagram "HUST" in the full-color imaging test (Figure 3h). Li et al. reported for the first time self-powered PDs based on the solution treatment of a $Cs_2AgBiBr_6$ double perovskite film.[67] Due to the high material integrity of $Cs_2AgBiBr_6$ and the effective interfacial charge transfer from perovskite to the bottom electron quenching layer, the PDs showed excellent performance. As shown in Figure 3j, the high-resolution image patterns were obtained by using the PDs as point-like sensor pixels. These results indicate that integrated image PDs can be successfully constructed by selecting different fabrication methods to achieve optical signal detection or color recognition. Ensuring the photoelectric performance of flexible perovskite devices while achieving device miniaturization and integration is a

significant technical challenge, mainly due to the incompatibility of perovskite materials with conventional lithography techniques and polar solution separation methods.[68,69] Therefore, there are stringent requirements on the quality of film formation and the crystallinity of the perovskite film itself. The strategies proposed in this study have the potential to be utilized for the large-scale fabrication of perovskite photodetector arrays, which can be beneficial for the advancement of integrated optoelectronic devices in the future. Additionally, this approach could enable the production of multispectral imaging arrays.

3. Fundamental Understanding of Perovskite Film in PDs

Due to the enormous application potential of metal halide perovskites in the fields of optoelectronics and photovoltaics, their structure and properties have been extensively studied.[40,70] Currently, most applications of perovskite-based PDs in optical communications and optical imaging are based on polycrystalline perovskite films. This is because the fabrication process is simple, the films easy to synthesize, and the fabrication cost is low. By optimizing the perovskite composition and film crystallinity, the optical response speed and detection capability can be improved, which is well applied in optical communication devices and imaging sensors.[2,71] Moreover, the PDs arrays with different structures, sizes and morphologies can be obtained by solution preparation processes.[72,73] In the preparation of metal halide perovskite films, a general distinction can be made between 3D perovskite films and quasi-2D perovskite films. 3D perovskite has extremely high photoelectric conversion efficiency but poor stability. Quasi-2D perovskite is a layered structure formed by the interweaving of organic and inorganic layers and is formed by dimensional reduction of 3D perovskite. The distinctive physical and chemical characteristics of quasi-2D perovskite materials make them an attractive alternative to 3D perovskite materials. Additionally, they exhibit improved environmental stability, making them imperative to carefully control the synthesis of quasi-2D metal halide perovskite materials. The manipulation of 3D perovskite films to create polycrystalline quasi-2D perovskite films has shown substantial progress. This section will focus on recent developments in the optical and photoelectric properties of both types of films, highlighting their potential applications in photoelectric systems.

3.1. PDs Based on 3D Perovskite Film

Polycrystalline 3D perovskite films are commonly used in the fabrication of perovskite photodetectors due to their ease of synthesis through the widely adopted spin-coating process and high quality results. In 2014, Hu et al. first reported flexible perovskite PDs with lateral structure based on a polycrystalline $MAPbI_3$ film,[4] which presented a spectral response of 3.49 A W^{-1}, an EQE of 1200%, as well as a wide wavelength range for optical response including the whole UV–vis region. Then, Dou et al. developed a vertical-structured film of polycrystalline $MAPbI_{3-x}Cl_x$ perovskite.[74] The resulting device demonstrated a remarkable specific detectivity of 10^{14} Jones, along with low noise current and rapid rise and decay times of 180 ns and 160 ns, respectively. These attributes render it highly suitable for optical communication and imaging applications. Following this, numerous studies have been conducted to enhance the photoelectric features of PDs based on polycrystalline perovskite films.[75–77] To ensure optimum performance in optical communication and image sensing applications, the fabrication of superior-quality perovskite films or film arrays is of utmost importance.

For instance, Cen et al. reported that $CsPbBr_3$ perovskite films with better orientation and larger grain size can be prepared on interfacial modified layer previously deposited by atomic layer deposition.[78] **Figure 4**a presents the SEM images depicting the film. The optimized $CsPbBr_3$ perovskite PDs exhibited exceptional performance due to the enhanced film quality and implementation of the double-sided interfacial technique. With a remarkably low dark current of 0.01 nA, high detectivity of 1.88×10^{13} Jones, and a wide linear dynamic range, as shown in Figure 4b, these PDs demonstrated remarkable efficiency. Finally, successful integration of the PDs within a visible light communication system was achieved (Figure 4c). As an optical receiver for text transmission, it had a bit rate of up to 100 kbps. Ma et al. optimized the quality of the photosensitive layer by using a suitable transmission layer, resulting in highly crystalline organic/inorganic hybrid $MAPbI_3$ perovskite PDs. Their devices presented a high sensitivity of 436 mA W^{-1} and a wide linear dynamic range (LDR) of 106 dB (Figure 4d), a fast response time of 1.7 µs, and a bandwidth of 75 kHz.[71] Due to their exceptional properties, perovskite PDs have been integrated into optical communication systems as optical sensors in the receiver terminal (Figure 4e). It enabled the successful, accurate, and fast transmission of strings, texts, and files by encoded light. The results indicate that organic/inorganic hybrid 3D perovskite-based PDs are highly promising for detecting visible light. These PDs, which can be easily integrated with optical communication devices, also hold great potential for optical image sensing applications. For example, Zhu et al. demonstrated the successful synthesis of high-quality Sn–Pb perovskite films with high crystallization. The researchers achieved this by first preparing dense nanocrystalline Sn–Pb perovskite films at room temperature, as illustrated in Figure 4f. The Sn–Pb perovskite film exhibited high crystal quality, resulting in reduced trap density and improved preferred orientation. Consequently, the fabricated perovskite photodetectors (PDs) demonstrated lower dark current and better power uniformity. To showcase the imaging capabilities, a 6×6 pixel image sensor was employed, and it successfully detected and displayed a clear "+" symbol in the corresponding photocurrent map. In a separate study conducted by Li et al., a novel X-ray image sensor was developed using a thick layer of lead-free $Cs_2AgBiBr_6$ double perovskite film. This innovative sensor showcased flexibility and the ability to capture images over a large area. Furthermore, the optical image of the $Cs_2AgBiBr_6$/polyvinyl alcohol (PVA) composite film, which had a thickness of 100 µm, was analyzed in this study. The cross-sectional scanning electron microscope (SEM) image of the film can be observed in Figure 4i. In order to produce the X-ray image sensor with detector arrays measuring 6×6 (as shown in Figure 4j), the authors utilized the Au layer as a contact electrode both prior to and subsequent to the evaporation of the film. The film underwent the application of silver paste islands via screen printing. The resulting sensor had an

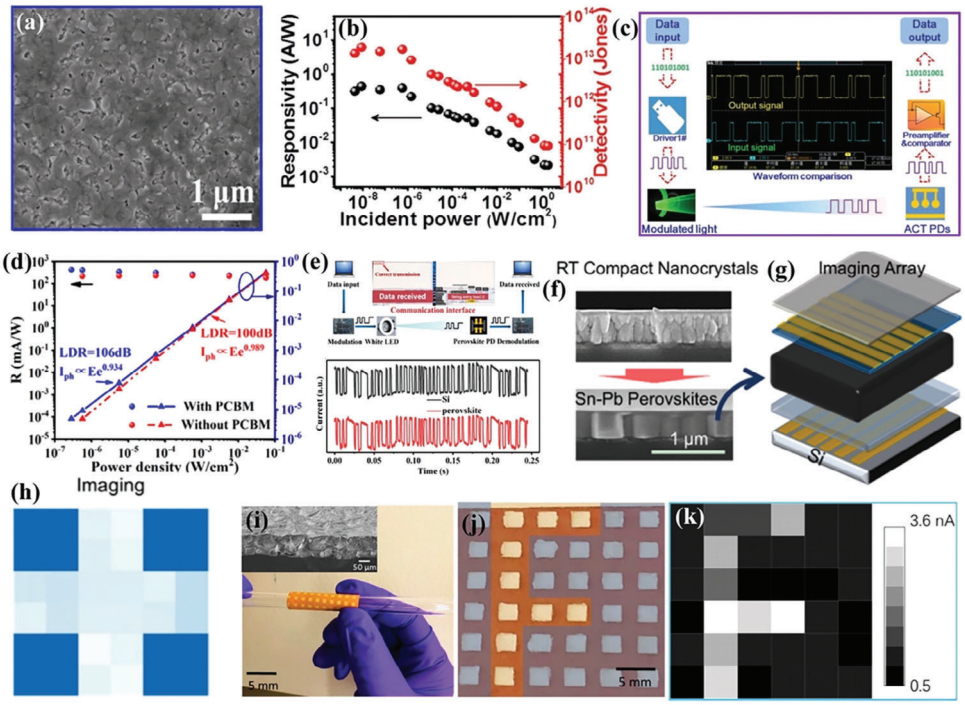

Figure 4. a) Plane-view SEM images of $CsPbBr_3$ perovskite films on FTO substrates. b) Responsivity and specific detectivity of PDs with different incident power. c) Schematic of the visible light communication system based on PDs (inset shows the waveforms comparison of PDs at 100 Hz). a–c) Reproduced with permission.[78] Copyright 2019, Wiley-VCH. d) Responsivity and photocurrent of PDs with different light intensities under 0 V bias. e) The schematic diagram of visible light communication (inset shows the communication interface when the signal "123456" is correctly transmitted), and the text data waveform received by the PDs. d,e) Reproduced with permission.[71] Copyright 2020, Springer. f) Cross-sectional SEM images of Sn–Pb perovskite films crystallized at room temperature without annealing (top) and with annealing (bottom). g) Schematic diagram of a vertical-structure imaging array based on perovskite film. h) Photocurrent mapping of the "+" optical image is output by the 6 × 6 PDs array. f–h) Reproduced with permission.[79] Copyright 2019, American Chemical Society. i) Optical image of a $Cs_2AgBiBr_6$/PVA composite film with a thickness of 100 μm. The inset shows a cross-sectional SEM image of a $Cs_2AgBiBr_6$/PVA composite film. j) Optical image of a $Cs_2AgBiBr_6$/PVA composite thin film X-ray image sensor with a 6 × 6 PDs array. k) Output the photocurrent mapping of the "F" type X-ray image. i–k) Reproduced with permission.[80] Copyright 2018, Royal Society of Chemistry.

ultrahigh sensitivity and excellent mechanical flexibility, and it did not show any significant performance degradation even when bent at large angles. Moreover, the $Cs_2AgBiBr_6$ film-based X-ray image sensor successfully detected the letter "F" with clear distinction of its pattern from the corresponding output photocurrent mapping (Figure 4k). These findings show that the film composed of lead-free double perovskite halides possesses considerable promise in the realm of adaptable X-ray visualization.

The timely and accurate response of perovskite PDs can be improved by effectively preparing perovskite films. To achieve future commercial applications of perovskite PDs, it is necessary to optimize existing methods or develop new methods with faster response times and higher resolutions. However, it is important to also consider the stability of perovskite materials when developing new methods to ensure success in achieving these goals.

3.2. PDs Based on Quasi-2D Perovskite Film

In order to guarantee coherence and uniformity in this examination, it becomes crucial to establish a clear definition for the concept of quasi-2D perovskite. Although prevailing literature often designates the stratified hybrid arrangement as 2D or quasi-2D perovskite, this terminology can be misleading as it might lead to confusion with the macroscopic shape of perovskite substances like nanoplates. Consequently, within the scope of this assessment, we shall adopt the term quasi-2D layered perovskite to explicitly denote the arrangement of the material, wherein the organic and inorganic layers alternate.[43,81,82]

The Ruddlesden–Popper (RP) phase, with general chemical formula $A''_2A_{n-1}Pb_nX_{3n+1}$, is a layered derivative of the perovskite family and is the most studied quasi-2D perovskite. It is arranged by monovalent organic spacer cations (A″) in a bimolecular layer, and the ammonium moiety points to the inorganic layer and is hydrogen bonded. The organic bimolecular layer is usually connected through van der Waals forces and π–π interactions. In organic bilayer, loose space is formed between relatively single ammonium cations, commonly known as the van der Waals gap. The metal halide plates are typically offset laterally by semi-octahedral unit, as shown in **Figure 5**a. Due to the inclination of the metal iodide octahedra, a strong deformation of the inorganic RP phase layer is usually reported.[86,87] In the perovskite structure, the value of n corresponds to the number of $[BX_6]^{4-}$ octahedra in each layer, which determines the thickness of the inorganic lattice. The perovskite structure undergoes a transition from a pure 2D phase to a combination of

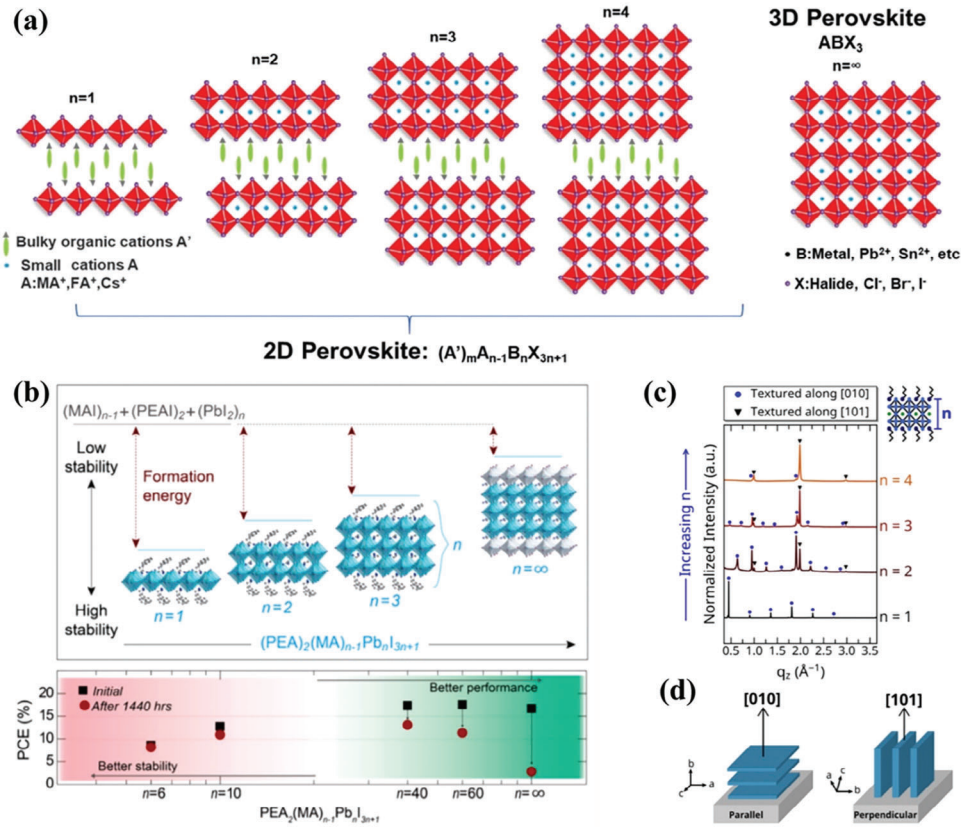

Figure 5. a) Comparison of 2D and 3D perovskite structures diagram (m = 2 in the figure). Reproduced with permission.[83] Copyright 2020, Royal Society of Chemistry. b) Schematic diagram of RP type perovskite structure changing with n value increasing from 1 to ∞, and the relationship between power conversion efficiency (PCE) and stability of RP type perovskite solar cell with n value. Reproduced with permission.[84] Copyright 2016, American Chemical Society. c) XRD of $(BA)_2(MA)_{n-1}Pb_nI_{3n+1}$ for n = 1 to 4. d) Diagram showing parallel and vertical crystallization orientation of PbI_2 plates. c,d) Reproduced with permission.[85] Copyright 2018, American Chemical Society.

2D and 3D perovskite, and eventually to a pure 3D phase as the n-value increases from 1 to ∞. This transformation is illustrated in Figure 5a.[83] Research indicates that the properties of RP perovskite are influenced by the variation in n value.[49,88] Figure 5b demonstrates that as n increases, the formation energy of RP perovskite decreases, suggesting that the pure 2D phase is more stable than the pure 3D phase.[84] Furthermore, the value of n also impacts the efficiency of the perovskite by adjusting its photoelectron properties. Specifically, a higher n value in RP perovskites results in an increase in the dielectric constant and a decrease in the exciton binding energy. Moreover, increasing the n value causes a reduction in the band gap energy (E_g). Additionally, the n-value significantly influences the crystal growth orientation, causing the orientation to approach that of the preferred 3D perovskite orientation.[44,89] For example, the film cast from solution, $(BA)_2(MA)_{n-1}Pb_nI_{3n+1}$ (BA = Butylammonium, $C_4H_{12}N$), exhibited a crystal texture of 2D PbI_2 layers that changed from parallel to the substrate (along the (010) texture) to perpendicular to it (along the (101) texture). This change was observed in Figure 5c,d and occurred for n values ranging from 1 to 4.[85] In contrast, there is a growing focus on quasi-2D perovskite-based PDs as they exhibit remarkable stability and convenient manipulation of photoelectric characteristics. These unique attributes make them highly suitable for optical communications and optical imaging, thus enhancing their application potential. Zeng et al. reported a kind of quasi-2D halide SA_2PbI_4 perovskite and corresponding PDs built with stearamine (SA, $C_{18}H_{39}N$),[90] a long-chain fatty ammonium series that is currently poorly developed. As shown in **Figure 6**a, it is waterproof, extremely low-noise, and has excellent photoelectric performance, making it highly suitable for underwater optical communications. Dimensional and component modulation can extend the absorption starting point to 1.5 eV and achieve a broadband response of full-spectrum optical underwater communication covering the entire transmission window of water (Figure 6b). The photodetectors (PDs) used in the experiment have a high sensitivity of 3.27 A W^{-1} and a maximum external quantum efficiency of 630%. They also have a fast rise/fall time of 0.35 ms/0.54 ms and can distinguish different waveforms and light intensities. These properties make them suitable for use in underwater environments, where they exhibited a sensitive and durable response to light. The successful demonstration of wireless transmission of ASCII code in water serves as a proof-of-concept for this technology (Figure 6c). In order to simulate the underwater mapping of the PDs array, they divided the multicolor image into 30 × 20 pieces and projected them onto the PD one by one, and then recorded the photocurrent and rearranged it to restore the original image with the correct sequence. The intensity of the surface is shown in Figure 6d, and it is clear

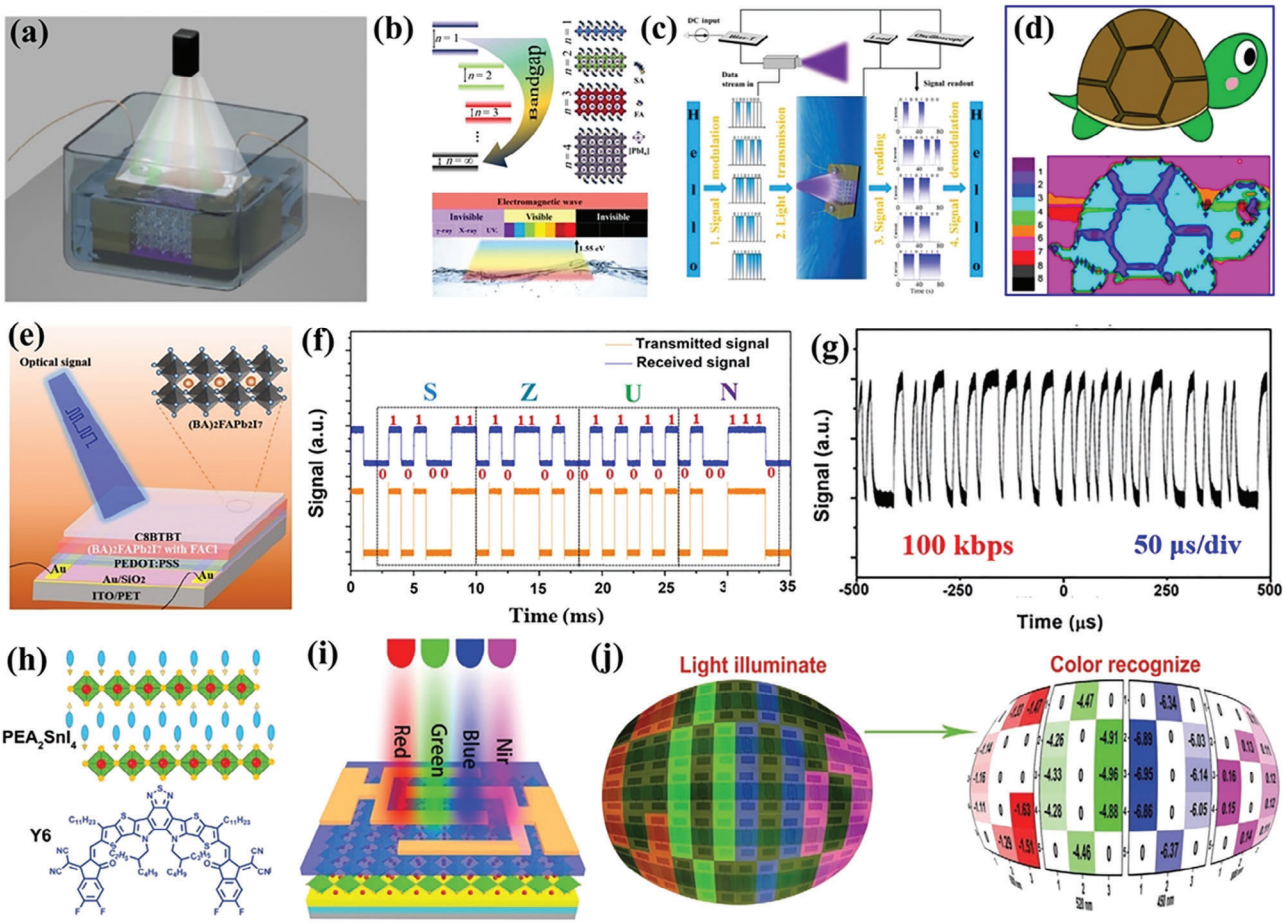

Figure 6. a) Schematic diagram of underwater imaging experimental facility. b) Quantum confinement effect in 2D HPs, schematic diagram of 2D HP structures with different inorganic [PbI_6] layer, and transmission spectrum of water. c) Signal modulation, optical transmission, signal reading, and signal demodulation of "Hello" ASCII codes. d) The mapping between the target image and the obtained one, the current unit is nA, the black color (bottom) indicates currents of >8.32 nA. a–d) Reproduced with permission.[90] Copyright 2021, Springer. e) Schematic illustration to measure the ultimate transmission rate of the PDs. f) The waveforms of electrical signal are obtained by one-chip computer and PDs. g) The PDs receives the waveform of digital data at transmission rate of 100 kbps. e–g) Reproduced with permission.[61] Copyright 2022, Wiley-VCH. h) Molecular structure of PEA_2SnI_4 perovskite and Y6. i) red, green, blue, and NIR light illuminate PDUs, respectively, j) LED light images of the 12 × 5 transistor arrays. Enter the letter "G," "o," "o," and "d," and the image consists of four 3 × 5 pixels encoded by red, green, blue, and NIR light, respectively. h–j) Reproduced with permission.[91] Copyright 2021, Wiley-VCH.

that the photocurrent mapping reproduces the target image in detail.

Wang et al. used FACl as an additive to improve the crystal quality of the film, and fabricated a self-supplied quasi-2D $(BA)_2FAPb_2I_7$ (n = 2) perovskite PDs with plasmonic heterojunction structure (Figure 6e).[61] The PDs utilized in this study demonstrated high sensitivity (2.3 A W^{-1}) and detectivity (3.2×10^{12} Jones), as well as fast response times (9.74 and 8.91 μs). An optical signal receiver was utilized to incorporate these PDs into a visible light communication system in order to transmit ASCII-encoded information (Figure 6f,g). The bit rate of transmission data was capable of reaching up to 100 kbps. This research marked the first investigation of formamidinium-based quasi-2D perovskite films in relation to optical communication. The findings demonstrate the potential applications of quasi-2D perovskite-based PDs in the realm of optical communications. The quasi-2D perovskite material's tunable band gap enables it to effectively respond to light within the near-infrared range, while the integrated PDs enable the detection and imaging of a wide-ranging spectrum. Huang et al. synthesized heterojunction films by combining Y6 with 2D perovskite PEA_2SnI_4 (PEA^+ = Phenethylammonium, $C_8H_{12}N$), which possesses remarkable photoelectric properties in the visible region.[91] The detection capabilities of the PDs were expanded to cover a wider range of wavelengths (300–1000 nm), allowing for detection in both the visible and near-infrared spectrum. The molecular structure of PEA_2SnI_4 and Y6 is depicted in Figure 6h. A flexible array of 12 × 5 pixels based on PEA_2SnI_4/Y6 was utilized for light-emitting diodes in four distinct colors, namely near-infrared, red, green, and blue, as illustrated in Figure 6i. The results indicate that the letters "G," "O," "O," and "D" were successfully identified with specificity.

At present, organic–inorganic hybrid perovskites are developing so rapidly that they are expected to replace commercial

silicon in the application of photodetectors in the near future.[12] Quasi-2D organic-inorganic layered perovskite-based PDs have been less studied than their 3D counterparts due to inferior performance and limited use in optical communication equipment and image sensors. However, they exhibit superior environmental stability, which is lacking in 3D perovskites. The photoelectric performance of quasi-2D perovskite films can be enhanced by reducing surface defect state and increasing crystallinity through various preparation methods. Thus, quasi-2D perovskite PDs exhibit immense promise in the domains of optical communication and imaging.

4. Strategies to Improve the Performance of Perovskite PDs

Perovskite photovoltaic materials, whether organic or inorganic halide-based, have shown great potential in the field. Nevertheless, the suboptimal crystal quality and inherent flaws of this material have substantial implications on device stability and overall performance. In this section, we present an extensive analysis of the main approaches utilized to ameliorate the photoelectric properties of perovskite films.

4.1. Composition Engineering

The molecular composition of perovskite plays a crucial role in the formation of the film, and therefore, modifying the components or introducing ion doping can improve film quality. Optoelectronic devices based on methylammonium lead iodide ($MAPbI_3$) have shown impressive performance in recent years.[16,17] However, $MAPbI_3$ exhibits poor moisture stability, thermal decomposition, and device hysteresis due to the weak interaction between polar $CH_3NH_3^+$ (MA^+) and inorganic PbI_3^- sublattice. To enhance water stability, MA^+ can be replaced by FA^+ or Cs^+. Additionally, replacing I^- with Br^- and/or Cl^- can expand the optical band gap of perovskite materials, allowing for wider absorption of the solar spectrum.[92] The unresolved issue of lattice strain in perovskite materials significantly affects their physical and device performance. A potential solution to this problem is adjusting the composition and proportion of perovskite to control lattice strain, which can result in the development of more efficient and stable devices. In a study conducted by Kong et al., the photoelectric properties of perovskite films were examined. The researchers prepared a variety of tri-cationic and mixed halide perovskite films and investigated the impact of lattice strain on these properties.[93] The schematic diagram in **Figure 7**a illustrates the relief of lattice strain in perovskite. Among the various perovskite films tested, the film composed of $(FAPbI_3)_{0.79}(MAPbBr_3)_{0.13}(CsPbI_3)_{0.08}$ showed exceptional performance in perovskite photodetectors (PDs). This particular film displayed an ultrahigh responsivity of 40 A W^{-1}, a detectivity of 1.9×10^{13} Jones, and an external quantum efficiency (EQE) of 9100% (Figure 7b). Furthermore, it exhibited superior stability. The study revealed that achieving optimal coordination between the elements in perovskite films can result in the release of lattice strain. This, in turn, contributes to the creation of thin films with fewer defects and longer carrier lifetimes. The findings highlight the significance of ion ratios in regulating lattice strain and determining the fundamental properties of perovskite optoelectronic devices. Therefore, researchers can utilize this understanding as a strategy for developing high-performance perovskite optoelectronic devices by using mixed-cationic lead mixed-halide perovskite. Wang et al. manufactured a PDs based on $FA_{(1-x)}Cs_xPb(Br_yI_{(1-y)})_3$ perovskite and revealed the effect of chemical composition on the stability of mixed cationic crystal phase and device performance.[94] The $FA_{0.7}Cs_{0.3}Pb(I_{0.8}Br_{0.2})$ PDs showed high specific detectivity (2.8×10^{13} Jones), which is the highest value to date for flexible perovskite PDs, and high responsivity and excellent stability under environmental conditions. These results show that mixed-cationic mixed-halide perovskite is expected to be applied in high-performance PDs and other flexible optoelectronic devices. To explore the correlation between optical stability and photoelectric properties of various phases, Wang et al. conducted a study on the crystal phase of a hybrid perovskite, $Cs_yFA_{(1-y)}Pb(Br_xI_{(1-x)})_3$, with mixed cationic lead and mixed halides.[95] Scientific evidence validates that the region between $0.10 < y < 0.30$ is determined to possess an elevated concentration of cesium. Furthermore, the film exhibits noteworthy attributes, including exceptional crystal quality, extended lifespan of carriers, and heightened mobility of carriers. The significance of high crystal quality in achieving satisfactory photoelectric quality and stable band gap has been well established. In order to identify the ideal cesium content, an investigation was conducted on the parameter space of $Cs_{0.17}FA_{0.83}Pb(Br_xI_{(1-x)})_3$ perovskite utilizing orthogonal halide variation (refer to Figure 7c). The perovskite system exhibited remarkable mobility and diffusion length of charge carriers throughout the entire iodide-bromide tuning range. As a result, the introduction of cesium led to the development of a perovskite system that is capable of stabilizing photosensitivity. This allows for fine-tuning of its absorption properties, ultimately optimizing the bandgap for photoelectric devices.

The regulation of organic spatial cations in RP-type quasi-2D perovskite has gained significant attention due to its ability to accommodate various functional groups and spatial structures. Different chain lengths and functional groups offer a variety of options for the selection of organic spatial cations in RP-type quasi-2D halide perovskite. These options encompass hydrophobic aliphatic alkylammonium cations (BA^+) and phenylaromatic alkylammonium cations (PEA^+), alongside with novel organic cations. This opens up possibilities for achieving new characteristics and enhancing performance.[31,38] Manipulating the crystallization kinetics is possible by adjusting the spacer cation type, which is a crucial factor. Such adjustments offer potential opportunities to enhance the film's quality in the perovskite of quasi-2D halide perovskite. For example, Shi et al. introduced a novel fluorine group, known as fluorine-substituted phenylethylamine (PEA^+), specifically 4-fluorophenylethylammonium ($4FPEA^+$, $C_8H_{11}FN$), as a spacer. They utilized this spacer to fabricate a quasi-2D $(4FPEA)_2(MA)_4Pb_5I_{16}$ ($n = 5$) perovskite film, employing a one-step spin-coating process based on the hot casting method. This approach proved to be more effective in comparison to the original PEA^+ cation.[96] The strong dipole field generated by the usage of $4FPEA^+$ organic space cation results in a noteworthy amplification in charge dissociation. Additionally, the enhanced functionality of the device can be credited to the modification in the perovskite film's quality. Figure 7d illustrates

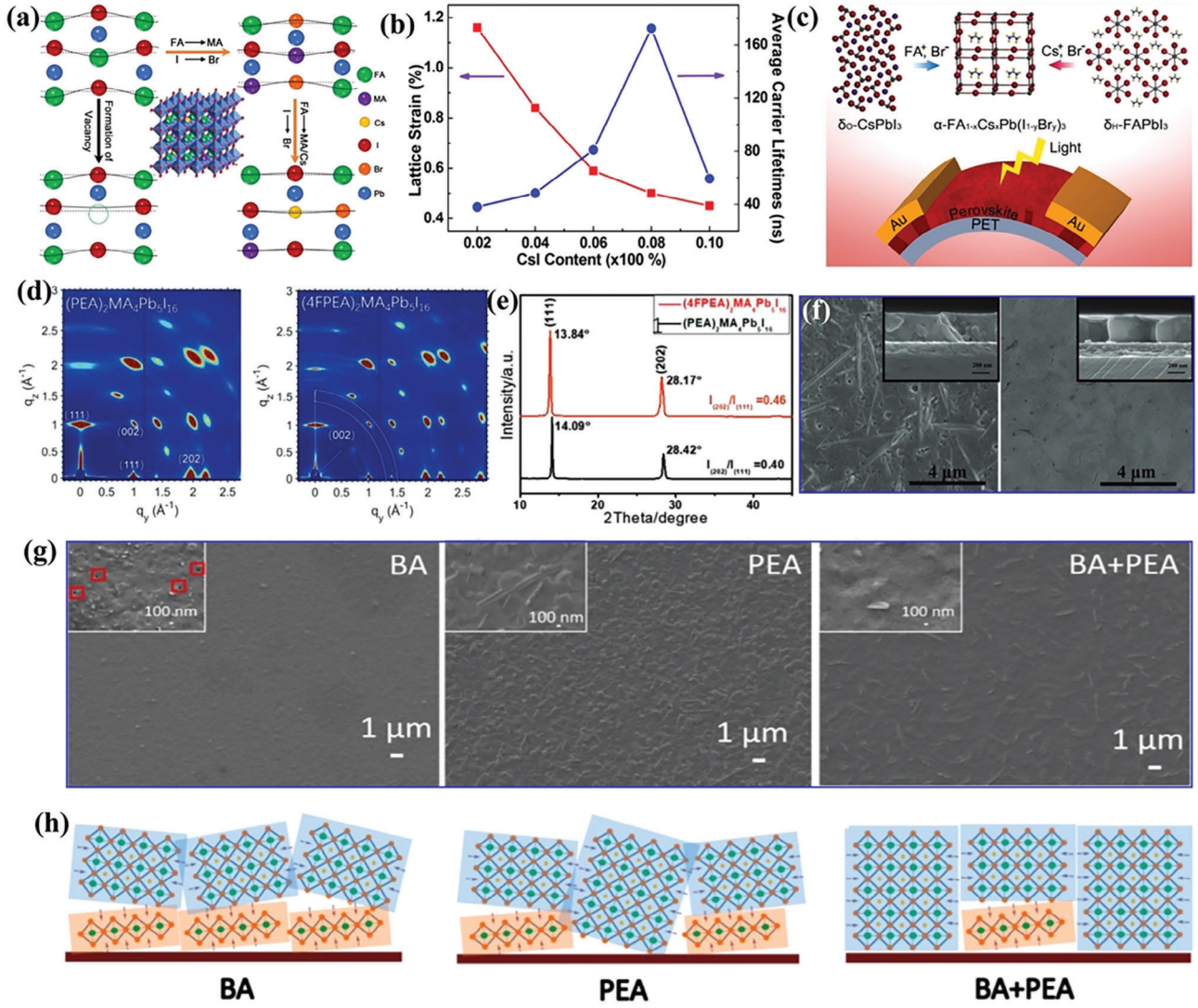

Figure 7. a) Schematic illustrations of lattice strain relief in $(FAPbI_3)_{0.79}(MAPbBr_3)_y(CsPbI_3)_{0.21-y}$ perovskite. b) Lattice strain and average carrier lifetimes of perovskite films with different CsI contents. a,b) Reproduced with permission.[93] Copyright 2022, American Chemical Society. c) Schematic diagram of the device structure of a perovskite PDs and ion replacement in perovskite lattice. Reproduced with permission.[94] Copyright 2019, American Chemical Society. d) 2D GIWAXS patterns, e) XRD patterns, and f) top-view and cross-sectional SEM images of $(PEA)_2MA_4Pb_5I_{16}$ and $(4FPEA)_2(MA)_4Pb_5I_{16}$ films. d–f) Reproduced with permission.[96] Copyright 2019, Wiley-VCH. g) Top-view SEM images of 2D RP Sn perovskite films, and h) schematic diagram of crystallization process of Sn-based RP perovskite films with BA^+, PEA^+, and BA^++PEA^+ as space cations. g,h) Reproduced with permission.[38] Copyright 2019, American Chemical Society.

that the $(4FPEA)_2(MA)_4Pb_5I_{16}$ perovskite crystals exhibit preferential growth perpendicular to the substrate, resulting in a favorable phase distribution. This distribution shows a normal gradient pattern, with the concentration of the phase increasing from the bottom to the top surface. Such a distribution promotes efficient charge transport. Moreover, the utilization of organic spatial cations ($4FPEA^+$) has been observed to enhance the film's crystallinity, enlarge the grain size, and mitigate the occurrence of trap states, as demonstrated in Figure 7e,f. One also used mixed spatial cations to flexibly manipulate the crystallization process to form high-quality films. Qiu et al. implemented the incorporation of mixed interval organic cations (namely BA^+ and PEA^+) in quasi-2D Sn perovskite in order to regulate the process of crystallization. The synergistic effect of the BA^+ and PEA^+ cations successfully hindered the occurrence of an intermediate phase induced by the oxidation of Sn^{2+}. This prevention was beneficial for promoting a homogeneous and ordered nucleation process. Ultimately, the regulation of the crystallization process of Sn-based quasi-2D perovskite led to the improvement of film morphology and crystal growth direction, along with the suppression of charge carrier recombination. This achievement is illustrated in Figure 7g,h.

4.2. Interface Engineering

Enhancing the efficiency of perovskite optoelectronic devices heavily relies on the optimization of the perovskite film's

quality. This can be achieved by selecting an appropriate underlying transport layer and modifying the underlying surface, which will improve the compatibility of the device configuration. Hybrid perovskites, which incorporate both organic and inorganic components, emerge as a favored option for achieving high-performance PDs primarily due to their impressive material characteristics. Nonetheless, the unregulated expansion of perovskite films along with sluggish charge extraction at the interface may curtail the sensitivity and response rate of PDs based on these materials. Despite the significance of this issue, there remains a paucity of investigations focusing on the influence of the electron transport layer (ETL) on PDs' response time. In their study on interface engineering strategy, Wang et al. conducted a performance comparison of perovskite PDs using TiO_2 and SnO_2 ETLs. One particular aspect of focus was the variation in photoresponse time.[97] Both PDs exhibited a significant difference in on–off current ratio, amounting to 10^5 and indicated a substantial detectivity of approximately 10^{12} Jones. The perovskite PDs, which relied on SnO_2, showcased an exceptional rise time of merely 3 µs accompanied by a corresponding decay time of 6 µs. Conversely, the perovskite PDs based on TiO_2 exhibited inferior responsivity and longer response time when subjected to lower driving voltage (**Figure 8**a). An electron extraction barrier existing at the interface between TiO_2 and perovskite, coupled with charge traps within the TiO_2 layer, can be responsible for this phenomenon. Moreover, the dark current of the PDs experienced effective suppression when a poly(vinyl pyrrolidone) interlayer was inserted. Consequently, an impressive enhancement in the on/off current ratio, amounting to 1.2×10^6 (as depicted in Figure 8b), was attained, corresponding to a tenfold amplification. Zhang et al. conducted a study where they introduced colloidal quantum dot of PbS combined with perovskite ($MAPbI_3$) as a crucial component in UV–vis–NIR broadband photodetectors (PDs).[65] To enhance the conductivity and improve the energy level matching of the PbS films, the PbS colloidal quantum dots were passivated with SCN^- anions through a solid ligand exchange technique. Figure 8c showcases the structure of the devices based on PbS/$MAPbI_3$ composites, along with a schematic representation of the ligands utilized for the exchange process. The composite PDs displayed a sensitive light response in the NIR region due to the complementary absorption spectrum and the effect of charge separation at the interface. Additionally, they demonstrated a significant improvement over the original $MAPbI_3$ or PbS colloidal quantum dot PDs in the UV–vis region. The PbS-SCN/$MAPbI_3$ composite PDs showed sensitivity to a wide range of wavelengths in the UV–vis–NIR region, with an impressive responsivity of 255 A W^{-1} and a fast response time of ≤42 ms. A successful development of a 10×10 array imager was achieved utilizing perovskite broadband PDs, demonstrating its potential as a high-performance image sensor capable of capturing a wide range of wavelengths and depicting detailed images (Figure 8d–f). These findings underscore the significance of interface engineering in enhancing the effectiveness of PDs.

Interface engineering has also been implemented on perovskite-based x-ray detectors. A study conducted by Demchyshyn et al.[98] focused on the creation of ultra-flexible, lightweight, and highly integrated X-ray PDs through the utilization of perovskite composed of a mixture of different cations and halide elements. The researchers achieved this by conducting thorough interface engineering research. In their study, they implemented five different inter-layer configurations (Figure 8g). The device operated successfully at 0 V, also known as passive mode. In this mode, the sensitivity was measured to be 9.3 µC Gy^{-1} cm^{-2}, with an effective area of 0.05 cm^2. The detection limit was found to be 0.58 + 0.05 µC Gy s^{-1}. In addition, these ultra-flexible devices allowed isotropic operation to reliably detect the back or front of the X-ray impact detector (Figure 8h). Mescher et al. developed an X-ray sensor that used a printable perovskite film with triple cationic composition (Figure 8i).[99] This device exhibits excellent X-ray stability, a low dark current, and a strong sensitivity of 59.9 µC Gy_{air}^{-1} cm^{-2}. In addition, the sputtered NiO_x hole transport layer was used to replace the spin-coated PEDOT: PSS through the interface engineering strategy, which demonstrated a significant reduction of dark current in detector. Figure 8k shows two typical cross-section SEM images of the studied hole transport layer. More obvious large columnar perovskite grains can be observed by using NiO_x as HTL.

To evaluate the X-ray imaging potential, a flexible X-ray detector incorporating a perovskite film was utilized for single-pixel imaging. The perovskite X-ray conversion layer's columnar grain structure is anticipated to minimize carrier losses occurring at the grain boundary due to non-radiative recombination impacts. The detector was used to detect objects that were affixed to the pneumatic joints and screws on the sample table (Figure 8l). As depicted in Figure 8m, the X-ray image clearly identifies different components of the object, demonstrating the outstanding X-ray imaging ability of the flexible X-ray detector based on perovskite film.

The application of PDs may be hindered by the undesirable confinement effect caused by quantum and the significant scattering of charge carriers at the interface in quasi-2D perovskite materials. In their study, Yu et al. introduced a new post-synthesis treatment using the interface engineering strategy. They focused on designing the dimension and interface of a 2D homologous perovskite film, which led to a significant enhancement in the performance of the corresponding visible light PDs. The quasi-2D $(OA)_2FA_{n-1}Pb_nBr_{3n+1}$ (OA^+ = Octadecylammonium, $C_{18}H_{40}N^+$) perovskite film, treated by immersing it in a solution containing FA^+, showed significant improvements. This treatment led to an increase in the dimension of the quasi-2D perovskite through the exchange reaction between OA^+ and FA^+, resulting in enhanced quantum confinement effect and improved separation of electrons and holes. Additionally, the treatment also caused independent quasi-2D perovskite nanocrystals to fuse together, which facilitated inter-domain carrier transport. These improvements in the perovskite film treatment are crucial for enhancing the performance and efficiency of optoelectronic devices. Figure 8n provides a visual representation of the increase in dimensionality and its impact on the electronic band structures. These advancements led to notable augmentation of the EQE and *R* of the treated PDs, reaching remarkable values of 4200% and 32 A W^{-1} respectively. Moreover, a substantial reduction by two orders of magnitude is observed in the rise/decay times, which amounts 0.25 ms/1.45 ms, respectively (Figure 8o).

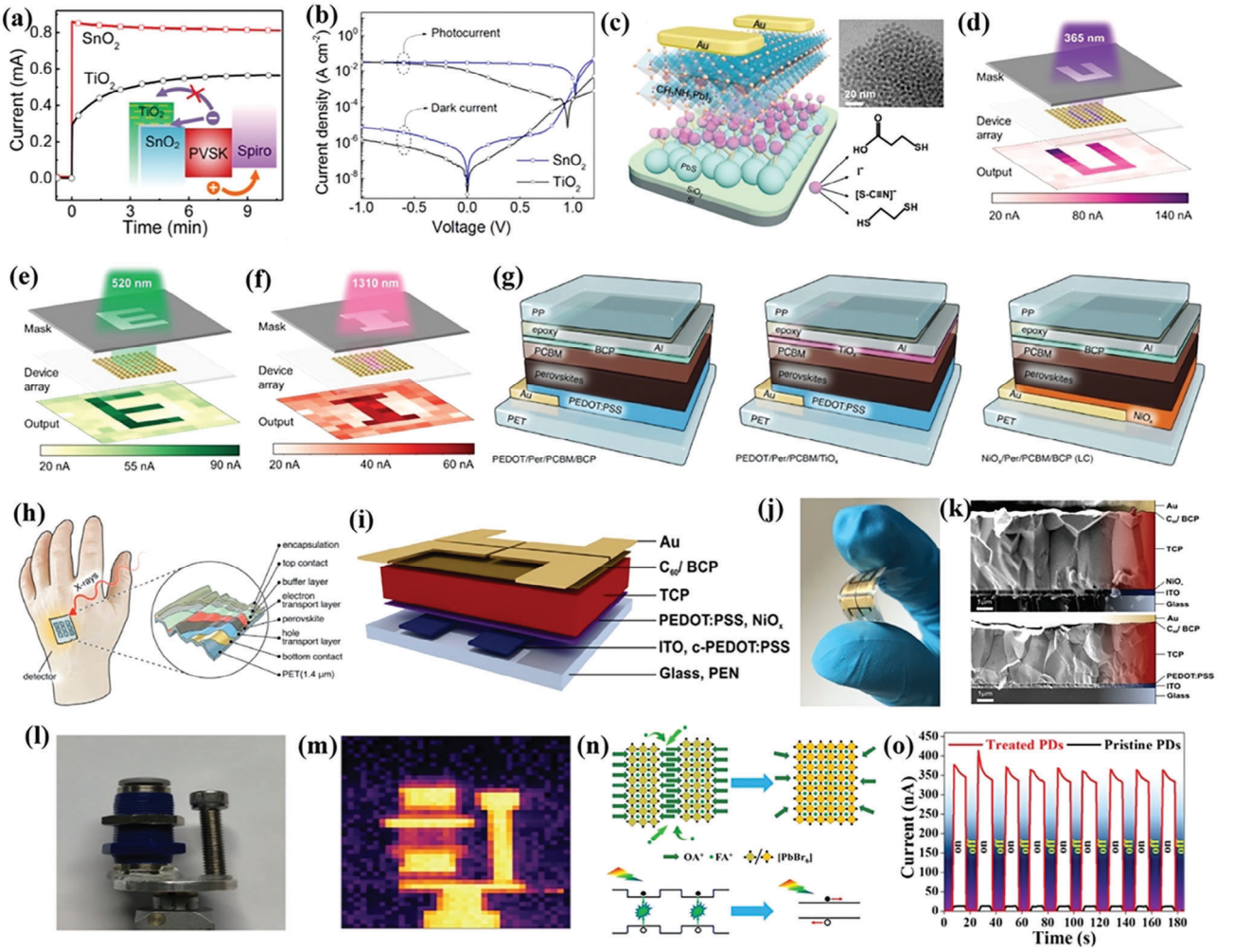

Figure 8. a) *I–t* curves and b) *J–V* curves of the SnO_2- and TiO_2-based perovskite PDs under the dark and 450 nm laser illumination with a light density of 100 mW cm^{-2}. The inset of Figure 7a shows the energy band diagram of TiO_2-based and SnO_2-based perovskite PDs. a,b) Reproduced with permission.[97] Copyright 2018, American Chemical Society. c) Schematic diagram of broadband PD device structure and switching ligand based on the PbS/$MAPbI_3$ composite. d) The imaging of the letter "U" under UV light, e) the image of the letter "E" under visible light, f) the image of the letter "I" under NIR light. c–f) Reproduced with permission.[65] Copyright 2019, American Chemical Society. g) Device structure at the interface between perovskite high energy photon absorber and PEDOT:PSS, PEDOT:PSS and PCBM/TiO_x, and NiO_x and PCBM/BCP using Al as the top contact and epoxy/polypropylene as encapsulation. h) Schematic diagram of 1.4 μm PET film perovskite X-ray detector. g,h) Reproduced with permission.[98] Copyright 2019, Wiley-VCH. i) Schematic diagram of flexible X-ray detector based on inkjet-printed perovskite film. j) Photograph of an X-ray detector based on flexible perovskite film. k) SEM cross-sectional images of a tricationic perovskite X-ray detectors printed by inkjet on rigid glass substrates based on NiO_x and PEDOT:PSS hole transport layers. l) Photograph and m) corresponding X-ray image of the pneumatic connector and screw mounted on the sample table. i–m) Reproduced with permission.[99] Copyright 2020, American Chemical Society. n) Schematic diagrams of the increases and consequent change in dimension of electronic band structures. o) *I–t* curves of the pristine and 30-min treated PDs. n,o) Reproduced with permission.[100] Copyright 2017, American Chemical Society.

4.3. Heterojunction Engineering

The photoelectric performance of PDs relies heavily on the quality of organic-inorganic hybrid perovskite. Key factors include the size of the grains, the ability to form films, and compatibility with other layers that serve various functions. One effective approach for boosting device performance involves the creation of a heterojunction structure. This can be achieved by introducing a modified layer alongside the perovskite layer. As a result, not only is the crystal quality of the perovskite enhanced, but the photoelectric response of the PDs is also significantly improved. Another strategy consist in combining perovskite with 2D materials, such as graphene or $PdSe_2$, which possess a high carrier mobility. This combination results in the formation of heterojunction PDs.

Xia et al. utilized chemical vapor deposition to deposit PbI_2 and MAI consecutively onto graphene, resulting in the formation of a van der Waals heterojunction between $MAPbI_3$ perovskite and graphene.[102] The perovskite $MAPbI_3$ grown through this technique exhibits dense crystal structure and large grain size, offering significant benefits for the fabrication of PDs with superior imaging capabilities. In this study, a PD based on $MAPbI_3$/graphene van der Waals heterojunction was

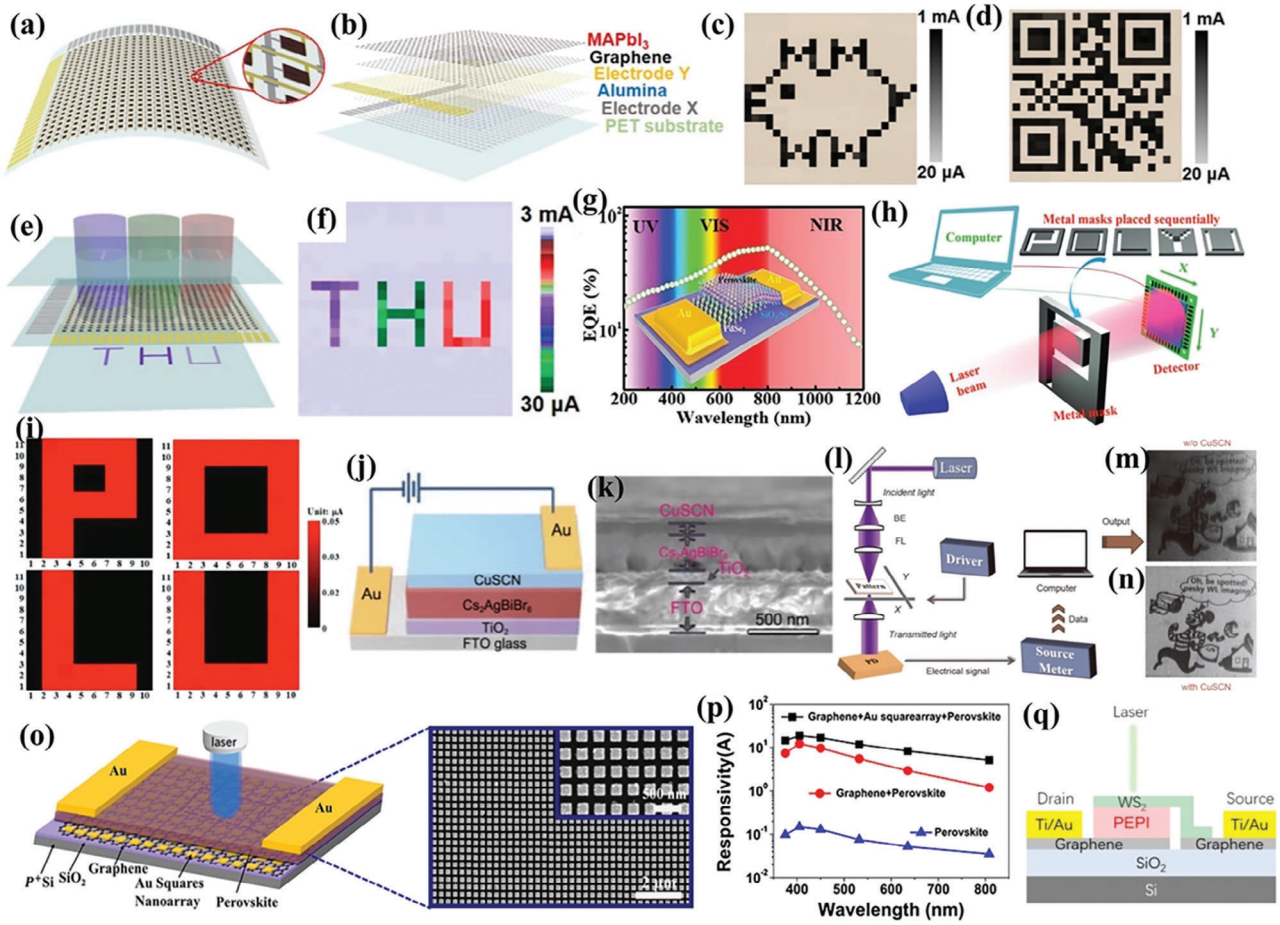

Figure 9. a,b) Schematic illustration of the flexible (24 × 24) pixels image sensor. c–f) The corresponding output images of a cartoon pig, 2D code, and letters "THU." a–f) Reproduced with permission.[102] Copyright 2020, Elsevier. g) EQE of $PdSe_2/FA_{0.85}Cs_{0.15}PbI_3$ perovskite PDs at different wavelengths. The inset is the schematic diagram of PDs. h) Schematic diagram of single-pixel imaging experimental equipment for $PdSe_2/FA_{0.85}Cs_{0.15}PbI_3$ PDs. i) Output photocurrent mappings of the letter patterns of "P," "O," "L," and "U" generated by the pattern masks under 808 nm illumination. g–i) Reproduced with permission.[103] Copyright 2019, Wiley-VCH. j) Schematic of the $Cs_2AgBiBr_6$-based PD. k) Cross-sectional view of the device. l) Self-built optical detection imaging system schematic diagram. Imaging results of the PDs m) without CuSCN layer and n) with CuSCN layer under 50 nW cm^{-2} illumination. j–n) Reproduced with permission.[104] Copyright 2020, Springer Nature. o) The PDs structure schematic and the SEM images of Au square nanoarray substrates. The inset shows different magnifications. p) Responsivity of PDs with different structures under 2 V bias under monochromatic light illuminations intensity of 0.25 μW cm^{-2}. o,p) Reproduced with permission.[105] Copyright 2021, American Chemical Society. q) Cross-section of a vertical heterostructure device with separate graphene layers, in contact with WS_2 monolayer and the $(PEA)_2PbI_4$ layer. Reproduced with permission.[106] Copyright 2022, American Chemical Society.

manufactured, demonstrating a high responsivity of 10^7 A W^{-1} and a response time of 50 ms. A flexible PDs array with 24 × 24 pixels was created to demonstrate its imaging capability (**Figure 9**a,b). The imaging results at a wavelength of 633 nm revealed clear and well-defined images of a cartoon pig, a 2D code, and the letters "THU" (Figure 9c–f). These results confirm the good imaging ability of the PDs array. Zeng et al. conducted a study on the preparation of a wideband PDs based on a $PdSe_2/FA_{0.85}Cs_{0.15}PbI_3$ Schottky junction.[103] The research findings indicated that the PD displayed a wide spectral range of response, a high ratio of light–dark current of ≈10^4, an impressive responsivity of 313 mA W^{-1}, an outstanding detectivity of 10^{13} Jones, and a rapid response speed of 4 μs. In order to assess the imaging ability of the $PdSe_2/FA_{0.85}Cs_{0.15}PbI_3$ Schottky junction PDs in near-infrared, a biaxial mobile platform (Figure 9h) was utilized for conducting single pixel imaging. The outcomes revealed that when subjected to 808 nm illumination, the corresponding output photocurrent mapping in Figure 9i accurately captured the letter patterns of "P," "O," "L," and "U." This finding highlights the superior near-infrared imaging capability of the $PdSe_2/FA_{0.85}Cs_{0.15}PbI_3$ Schottky junction PDs. In order to enhance the imaging performance under weak scattering light, it is important to find a suitable hole transport layer and apply it to perovskite PDs. A recent study utilized all inorganic $Cs_2AgBiBr_6$ PDs with CuSCN as the hole transport layer for low-light imaging.[104] The device structure consisted of $Cs_2AgBiBr_6$/CuSCN (Figure 9j,k). According to the findings, the utilization of CuSCN as a layer for transporting holes greatly enhanced the extraction and transportation capacity of carriers in PDs, consequently resulting in improved imaging performance.

The imaging capability of $Cs_2AgBiBr_6$ PDs was proven to be exceptional even in low-light settings through the utilization of a self-constructed laser scanning imaging system. The PDs were able to clearly identify images even at a light intensity as low as 5 nW cm^{-2} (Figure 9l–n). The findings indicate that imaging applications can greatly benefit from the utilization of all-inorganic perovskite PDs fabricated using bismuth (Bi), especially when incorporating appropriate heterojunction architectures.

The improvement of light absorption and charge mobility in quasi-2D perovskite polycrystalline films has been hindered by the presence of grain boundary defects. These defects limit the photocurrent and ultimately reduce the efficiency of the films. To overcome this challenge, Wang et al. have developed a new type of perovskite film called broadband 2D/quasi-2D $(BA)_2(FA)_{n-1}PbnI_{3n+1}$ (n = 1 or 2) perovskite PDs. These films not only exhibited strong light trapping capabilities but also demonstrated good stability. This was achieved by combining both the Au square nanoarray and a monolayer of graphene.[105] In Figure 9o, it can be observed that the implementation of graphene and Au square nanoarrays in the interface engineering strategy leads to enhanced crystal quality, carrier mobility, and light absorption of the film. Additionally, this approach maximizes light trapping, electromagnetic field enhancement, and light-induced carrier extraction. As a result, there is a substantial increase in the photocurrent of the device within the visible and near-infrared range. Comparatively, the responsivity and detectivity of the device, when solely based on perovskite in PDs, were two orders of magnitude lower (Figure 9p). In addition, Wang et al. proposed a WS_2 single layer/$(PEA)_2PbI_4$ 2D perovskite vertical van der Waals heterostructure PDs.[106] The device structure diagram is depicted in Figure 9q. The PDs demonstrated a short circuit current of 41.6 nA. At the heterointerface of WS_2/$(PEA)_2PbI_4$, a photoresponsivity of 0.13 mA W^{-1} was achieved, which was 5 times higher than that of an individual WS_2 region. This study validates that 2D perovskite holds potential as a light-absorbing layer for optoelectronic devices with transition metal dihalide heterogeneous interfaces.

4.4. Film Crystallinity Improvement Engineering

The organic–inorganic hybrid perovskite PDs exhibit exceptional device performance, thanks to their excellent material properties. Moreover, the noteworthy potential of halide perovskite-based devices as an economical alternative to current light-harvesting materials in commercial applications is highlighted by their ability to be processed affordably. However, the utilization of solution treatment processing for the fabrication of perovskite polycrystalline films often results in films that are not compact, exhibit inadequate crystallization, pose challenges in controlling crystallization nucleation, and display structural, chemical, and grain boundary issues. These problems significantly hinder the photodetection efficiency of PDs. Hence, it becomes imperative to address the underlying issue of perovskite film development and adopt techniques and approaches to enhance its crystallinity. By doing so, we can significantly enhance the photoelectric efficiency of devices based on perovskite materials, leading to their wider range of applications. Through the utilization of non-fullerene passivation, an effective method for the passivation of perovskite materials is demonstrated. This approach exhibits remarkable reduction in trap state density, thereby enhancing the quality of film formation.[107] Consequently, a remarkably low dark current of 2.6×10^{-8} A cm^{-2} at −0.1 V is achieved. Moreover, the passivation of perovskite photodetectors (PDs) yields a substantial broadening of their optical response range, extending beyond 900 nm. The net result of this enhancement is a specific detectivity of 1.45×10^{12} Jones at 650 nm, coupled with an exceptional response speed of 27 ns. This showcases the remarkable practical applications of PDs in weak light detection circuits and visible light communication systems.

We now focus on discussing the advancements in film crystallinity engineering. In the next section, we introduce in detail the strategies and methods implemented to improve perovskite films.

5. Strategies for Increasing Crystallinity of Perovskite Films

In the production of perovskite films, the enhancement of film quality often involves the simultaneous implementation of multiple strategies. It is imperative to evaluate the collaborative efforts of these strategies and their respective roles in the process. Their interaction and their collective influence on film quality during the formation of perovskite films necessitate the adoption of a combination of diverse techniques to optimize film quality. Our focus in this section is primarily on the engineering of additives and post-treatment to elevate the morphological and crystal quality of perovskite films and enhance the functionality of optoelectronic devices.

5.1. Additive Engineering

While underlayer engineering and heterojunction engineering have the potential to enhance film quality, the task of finding a compatible interface layer for perovskite remains a challenge.[108,109] Therefore, it is crucial to explore alternative approaches to control crystal growth. Additive engineering has emerged as a successful strategy for optimizing the perovskite layer, leading to improved efficiency and stability in perovskite devices. Consequently, numerous substances have been recognized for their efficacy in regulating the process of halide perovskite film formation.

5.1.1. 3D Perovskite Films

Along with molecular incorporation in a perovskite precursor, there have been many reports on solvent additives to the 3D perovskite.[110] Li et al. investigated the utilization of polyethylene glycol (PEG, $C_{2n}H_{4n+2}O_{n+1}$) as an additive in order to passivate localized defects in $CsPbI_2Br$ films via a Lewis acid–base interaction.[111] To achieve this, a small amount of PEG additive with a concentration of 0.4 mg mL^{-1} was introduced into the $CsPbI_3$ precursor (**Figure 10**a,b). The addition of PEG efficiently passivates the interface defects, as evidenced by the remarkable reduction in trap density of states, as observed through

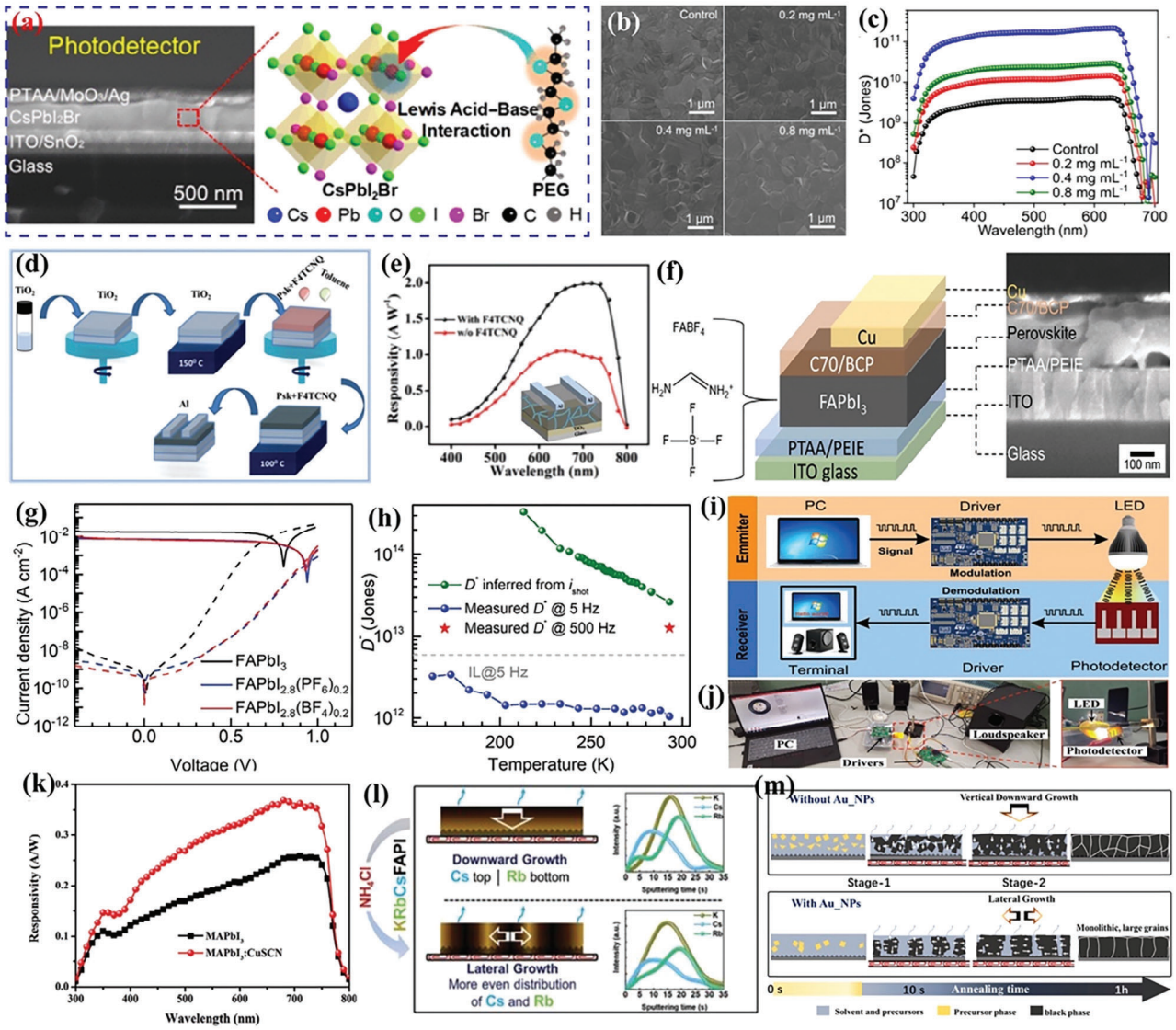

Figure 10. a) Cross-sectional view of the device and illustration of Lewis acid–base interaction between uncoordinated Pb^{2+} and PEG. b) SEM images of the $CsPbI_2Br$ films modified with different concentrations (0, 0.2, 0.4, 0.8 mg mL^{-1}) of PEG. c) Specific detectivity of PDs. a–c) Reproduced with permission.[111] Copyright 2021, American Chemical Society. d) Schematic illustration of device fabrication incorporated with F_4TCNQ. e) Responsivity of PDs with/without F_4TCNQ incorporation at bias of 5 V and 10.6 mW cm^{-2} illumination. The inset shows the structure of the PDs. d,e) Reproduced with permission.[114] Copyright 2020, Royal Society of Chemistry. f) Device structure diagram and cross-sectional SEM image of pseudohalide enhanced perovskite photodiode. g) *J–V* curves in dark and 1 Sun white light illumination of device. h) specific detectivity of the optimized $FAPbI_{2.8}(BF_4)_{0.2}$ perovskite PDs. f–h) Reproduced with permission.[115] Copyright 2020, Wiley-VCH. i) Schematic diagram of a visible light communication system with transmitter and receiver subsystems. j) Home-made visible light communication system photograph based on perovskite PDs. k) Responsivity of the PDs based on $MAPbI_3$ and $MAPbI_3$:CuSCN. i–k) Reproduced with permission.[59] Copyright 2020, Wiley-VCH. l) Distribution diagram of multiple ions in KRbCsFA perovskite layer without and with NH_4Cl preparation and corresponding film forming process. Reproduced with permission.[116] Copyright 2022, Wiley-VCH. m) Thermal annealing film formation of Ref and Au_NPs-30 samples: direction and mechanism of grain growth. Reproduced with permission.[117] Copyright 2022, Elsevier B.V.

thermal admittance spectroscopy. Fourier transform infrared spectroscopy analysis revealed the formation of Lewis acid–base interactions between Pb^{2+} and PEG, resulting in the passivation of defects in $CsPbI_2Br$ perovskite and suppression of noise currents. This passivation strategy leads to excellent photoelectric detection performance in all inorganic perovskite photodetectors, with a specific detectivity of 2.2×10^{11} Jones and an LDR of 116 dB (Figure 10c). Taken together, these findings demonstrate the potential of utilizing the environmentally stable polymer additive PEG to passivate defects and achieve superior photoelectric detection performance in all inorganic perovskite photodetectors. Subsequently, Wang et al. used $Ti_3C_2T_x$ MXene for additive engineering of $CsPbI_2Br$ perovskite.[112] The inclusion of MXene greatly enhanced the crystallinity of perovskite films while reducing the occurrence of defects. Furthermore, the creation of Schottky junctions between $CsPbI_2Br$ and MXene nanosheets

improved the separation and transfer of electron–hole pairs generated by light, ultimately leading to the best possible incorporation of MXene. That is, compared to the control device without MXene added, the relative performance increased by about 16.7%. Divalent metal chloride salts ($SrCl_2$ and $NiCl_2$) can also be used as additives to regulate $CsPbI_2Br$ perovskite and enhance the formation of high-quality perovskite films.[113] Based on the experimental findings, it is evident that this approach has the capability to yield films of exceptional quality, elevate the electronic characteristics, eradicate any faulty states, and prolong the lifespan of carriers. These additives strategies will provide new insights into the controllable manufacture of highly efficient all inorganic perovskite optoelectronic devices.

The introduction of small organic molecule F4TCNQ into the perovskite solution ($Cs_{0.1}FA_{0.2}MA_{0.7}Pb(I_{0.9}Cl_{0.1})_3$) has been found to induce several positive effects on the perovskite films. It promotes the reduction of metal lead defects and grain boundaries, leading to improved crystal quality. Additionally, the presence of F4TCNQ increases the grain size of the perovskite, which also contributes to enhanced crystal growth. Furthermore, the use of F4TCNQ has been shown to improve the carrier lifetime of the perovskite films, indicating better performance and stability. Overall, the addition of F4TCNQ in the organic–inorganic hybrid perovskite helps in defect passivation, promotes crystal growth, and enhances the performance of the perovskite films. They improves the morphology of the film and improve the performance of PDs.[114] Figure 10d illustrates the diagram for device fabrication where F4TCNQ is integrated. The performance of the device is enhanced when the optimal F4TCNQ ratio is used, in contrast to the control device lacking F4TCNQ. The photodetector device with an F4TCNQ concentration of 5 vol% exhibited a responsivity of 5.41 A W^{-1} along with an on/off ratio of 7000 (as shown in Figure 10e). Additionally, the PDs device demonstrated remarkable stability for a period of 25 days in ambient conditions.

The inclusion of pseudo-halide salts has emerged as a promising technique to enhance the long-term stability of devices. It has been observed that these pseudohalide ions effectively act as passivators for the device grains, successfully impeding their degradation. Li et al. conducted a study on the introduction of pseudohalide additives, specifically BF_4^- (Tetrafluoroborate) and PF_6^- (Hexafluorophosphate) anions, into $FAPbI_3$ perovskites. They fabricated perovskite photodetectors (PDs) using these modified perovskites.[115] The $FAPbI_{2.8}(BF_4)_{0.2}$ film demonstrated excellent crystallinity and air stability, effectively inhibiting the formation of the δ phase of $FAPbI_3$ perovskite. The modified perovskite PDs exhibited significantly reduced dark current and noise compared to the original $FAPbI_3$ devices and devices based on $MAPbI_3$ and tri-cationic perovskite (Figure 10g). Unlike the temperature dependency seen in the original devices, the perovskite PDs with pseudohalide additives showed less temperature dependency. Furthermore, the modified perovskites demonstrated an ultrafast response time of approximately 50 ns and a relatively high detectivity of over 10^{12} Jones (Figure 10h). These findings highlight the potential of pseudohalide modified perovskites in enhancing the performance of perovskite PDs, particularly in terms of reducing dark current and noise, improving temperature stability, and achieving high responsiveness and detectivity. In addition, Liu et al. proposed a strategy for $CuSCN^-$ induced p-type doping of $MAPbI_3$ perovskite film. This strategy aimed at enhancing hole transport, mitigate trap states, prevent charge accumulation, suppress photogenerated carrier recombination, and notably enhance the photoelectric performance of self-powered hole-free conductor devices.[59] The most favorable device exhibited a maximal responsivity of 0.37 A W^{-1} (Figure 10k), a detectivity of 1.06×10^{12} Jones, an extensive LDR surpassing 100 dB, and an ultimate photo-response rate approaching 5 µs. Furthermore, the optimized perovskite photodetectors were seamlessly incorporated into a custom-designed visible light communication system to function as an optical signal receiver, offering promising applications in text and audio signal transmission (Figure 10i,j).

Our group has also done a lot of work to optimize the film quality through different additives.[110,117–120] For example, it conducted an investigation of the impacts of alkali metal cations ($K^+/Rb^+/Cs^+$) and ammonium chloride (NH_4Cl) additives on the formation process of methylamine-free, formamidine iodized perovskite films. The outcomes demonstrated that the addition of NH_4Cl promotes the solubility of PbI_2 in the solution through the creation of intermediates, resulting in favorable conditions for the development of the perovskite phase.[116] Furthermore, NH_4Cl can increase grain size, improve crystallinity, and inhibit the formation of PbI_2 during annealing. At low concentrations, potassium (K) is evenly distributed throughout the film thickness, while cesium (Cs) is more concentrated on the surface and rubidium (Rb) is more concentrated deep in the original layer. However, after the addition of ammonium chloride (NH_4Cl), the distribution of these two alkali metals becomes more uniform. The presence of NH_4Cl decelerates the motion of Cs^+ and Rb^+ ions, thereby modifying the orientation of perovskite films and enhancing the overall quality of crystallization, consequently leading to a homogeneous distribution (Figure 10l). As a result, perovskite films exhibited extensive, contiguous grains. It is also reported that using a coadditive method to mix two chlorides (potassium chloride (KCl) and NH_4Cl) in a perovskite precursor solution, the synthesized $Cs_xFA_{1-x}PbI_3$ perovskite without methylammonium and bromine has intrinsic excellent performance in crystallinity, defect elimination/passivation, and ionic mobility blocking.[119] The crystal growth rate can be managed by NH_4Cl, leading to the generation of substantial grains and layers that are well-crystallized. The application of the glow discharge optical emission spectroscopy technique (GD-OES) enabled us to directly observe potassium dispersed within the film, which effectively hindered the migration of iodide through the passivation of defects. Additionally, there is a strong correlation between the reduction (or prevention) of iodide mobility and the decline (or prevention) of *J–V* curve hysteresis. It was found that preventing ion migration was not enough to make the halide perovskite material completely stable, and a second additive was required for parallel crystal monitoring. We also introduce Au nanoparticles (Au_NPs) into $MAPbI_3$ to improve the quality of perovskite films.[117] Through the utilization of a range of analytical methods, specifically employing GD-OES, we elucidated the underlying process by which Au_NPs enhance the overall quality of perovskite films. The presence of Au_NPs facilitates the creation of coherent grain structures characterized by minimal flaws and limited grain junctions, a vital aspect for achieving heightened efficiency (Figure 10m). Consequently, within our experimental setup, the impact of Au_NPs on enhancing the perovskite layer's quality surpasses the influence of enhanced light absorption.

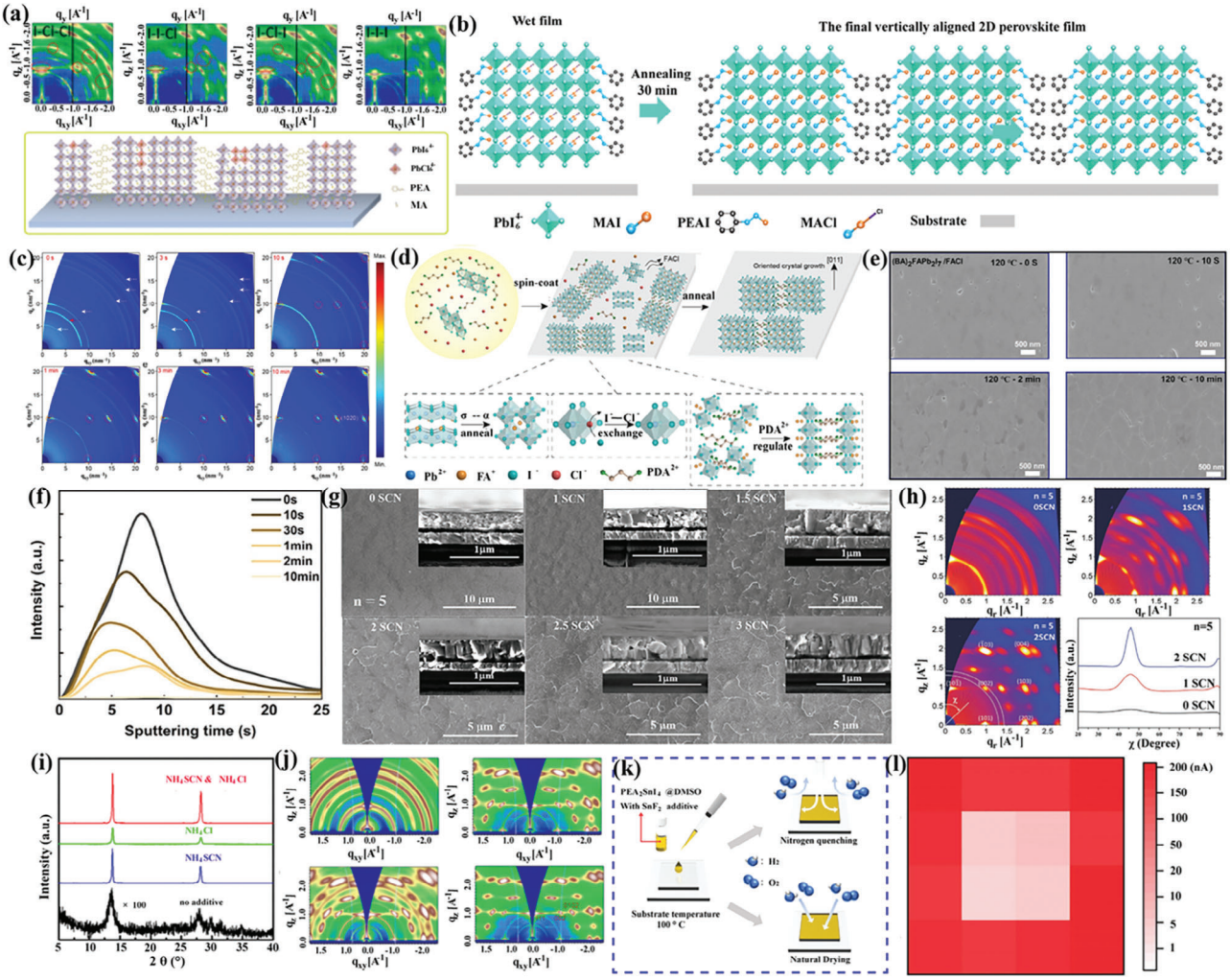

Figure 11. a) GIWAXS images and crystal orientation of perovskite films. The characteristic peaks of chloride containing systems are represented by red rings. Reproduced with permission.[124] Copyright 2019, Elsevier B.V. b) Vertical alignment of quasi-2D perovskite growth process diagram. Reproduced with permission.[125] Copyright 2020, Elsevier B.V. c) Quasi-2D GI-XRD pattern of perovskite films after annealing at 150 °C for 0 s, 1 min, and 10 min, respectively. The red dot arrow indicates the Delta-phase $FAPbI_3$, the white dot arrow indicates the Cl-containing intermediate, and the orange circle indicates the Bragg peak location of the $(PDA)(FA)_3Pb_4I_{13}$ perovskite. d) Microscopic growth mechanism of quasi-2D perovskite films assisted by FACl. c,d) Reproduced with permission.[22] Copyright 2021, Wiley-VCH. e) Top view of SEM images of $(BA)_2FAPb_2I_7$ perovskite films with 8 mg mL^{-1} FACl annealed at 120 °C for 0 s, 10 s, 2 min, 10 min, respectively. f) GD-OES chloride profile evolution with increasing annealing time. e,f) Reproduced with permission.[61] Copyright 2022, Wiley-VCH. g) Top-view SEM images with cross-sectional SEM images. h) 2D GIWAXS patterns, and polar intensity profiles along the ring in the q_r of $(PEA)_2(MA)_4Pb_5I_{16}$ perovskite films fabricated with different amounts of NH_4SCN. g,h) Reproduced with permission.[126] Copyright 2022, Wiley-VCH. i) X-ray diffraction of the perovskite films prepared with various additives. j) GIWAXS diagram of perovskite films prepared with various additives. i,j) Reproduced with permission.[127] Copyright 2018, American Chemical Society. k) Schematic diagram of a nitrogen quenching hot casting fabrication process to prepare PEA_2SnI_4 films. l) 4 × 4 PDs array corresponding image-sensing profiles of letter "O." k,l) Reproduced with permission.[128] Copyright 2022, Wiley-VCH.

5.1.2. 2D Perovskite Films

Recent studies have shown that functional additives commonly used for 3D inorganic perovskite formation can also be used to manipulate the formation process of quasi-2D perovskite. These additives, such as methylammonium chloride (MACl), formamidine chloride (FACl), and ammonium chloride (NH_4Cl), have been utilized by researchers to prepare high-quality quasi-2D perovskite films. Using these chloride salts as additional film-forming technologies has led to an augmentation in grain size, improved crystallinity, and the attainment of a uniform and sleek surface.[86,121–123] Despite the widespread use of MACl and FACl to enhance the performance of quasi-2D perovskite devices through enhancements in morphology and crystallinity, the precise role of MACl and FACl, particularly the impact of chloride ions (Cl^-) in the film formation process, remains unclear and subject to debate. Previous research has suggested that MACl serves as a valuable source of organic ammonium salts, wherein Cl^- is incorporated to produce Cl-doped layered perovskite films, as depicted in **Figure 11**a.[124] However, additional investigations have presented evidence indicating that MACl or FACl merely functions as an auxiliary additive,

facilitating the formation of intermediate phases during the creation of quasi-2D perovskite films, with Cl^- being absent in the final film composition. MACl or FACl can induce the formation of an intermediate phase comprised of perovskite crystals without the need for annealing during the formation of layered $PEA_2MA_4Pb_5I_{16}$ films facilitated by MACl and perovskite films (Figure 11b–d) facilitated by FACl. This method directly enhances the alignment of quasi-2D perovskite films on substrates that have been annealed.[22,125] In the film preparation process (Figure 11e), Wang et al. incorporated FACl as an additive, leading to a significant enhancement in the quality and crystallinity of quasi-2D $(BA)_2FAPb_2I_7$ perovskite films.[61] To investigate the role of Cl in this process, GD-OES analysis was conducted. Through annealing, the Cl-containing intermediates present in the transition state were eliminated (Figure 11f). As a result, the perovskite films exhibited extensive crystallization, a smooth and defect-free surface, and excellent photoelectric properties. It should be emphasized that precise control of the concentration of the Cl additive is crucial in order to achieve the highest device performance for quasi-2D perovskite films. Excessive addition of Cl sacrifices the smoothness and compactness of the film surface, thereby diminishing the performance of the devices.

Quasi-2D perovskite films regulated by thiocyanate salts are also popular additives. Thiocyanates salts, such as ammonium thiocyanate (NH_4SCN), have been commonly used as additives in the formation of high quality quasi-2D perovskite films. The thiocyanate ion (SCN^-) has a similar ionic radius to that of the halide ion (I^-), allowing it to replace the halide ion in the perovskite structure. Furthermore, the thiocyanate ion can interact strongly with Pb^{2+} through its S and N atoms which possess lone electron pairs. These characteristics of SCN^- make it an effective additive for facilitating the perovskite film formation process. Zhang et al. conducted a study in which they utilized a one-step spin-coating method to prepare quasi-2D perovskite films with the assistance of an ammonium thiocyanate (NH_4SCN) additive.[126] By incorporating this additive, they were able to create vertically oriented and highly crystalline films, which resulted in improved performance of the devices. The addition of NH_4SCN also influenced the grain orientation of the films, as seen in Figure 11g. Without NH_4SCN, the film had randomly oriented small grains. However, with increased NH_4SCN addition, the grains transformed into highly ordered brick-like structures with perpendicular orientation to the substrate. This transformation was further confirmed by the 2D GIWAXS analysis shown in Figure 11h, which clearly demonstrated the enhanced directional ordering of crystals after incorporating NH_4SCN.

To enhance the performance of devices, Fu et al. employed NH_4Cl and NH_4SCN as additives and documented a remarkably efficient quasi-2D perovskite device based on $(PEA)_2(MA)_4Pb_5I_{16}$. The preparation of perovskite layers involved the simultaneous use of additives NH_4Cl and NH_4SCN.[127] The study's results demonstrate that NH_4SCN and NH_4Cl have varying effects on the perovskite films synthesized, as indicated in Figure 11i. NH_4SCN is primarily responsible for enhancing crystallinity and regulating crystal growth along the vertical direction. On the other hand, NH_4Cl plays a significant role in managing film compactness and uniformity, as shown in Figure 11j. The $(PEA)_2(MA)_4Pb_5I_{16}$ films demonstrate superior characteristics when their advantages are combined together. These advantages include high crystallinity, excellent compactness and uniformity, and a preference for vertical growth direction. Additionally, the devices show excellent photoelectric conversion efficiency.

Undoubtedly, there are many different types of additives that can be used to match particular types of quasi-2D perovskites to improve the film crystallinity. Tin halide perovskites have emerged as a potential alternative to Pb-based perovskite in various applications, mainly because of their low toxicity and potential for commercialization. However, their instability in the presence of air poses a significant challenge. The oxidation of Sn^{2+} to Sn^{4+} greatly compromises the performance of devices based on tin halide perovskite and also hinders the manufacturing process in air. This self-doping effect leads to rapid degradation of device performance and the difficulties in fabricating tin halide perovskite-based devices in air need to be addressed for the material to realize its full potential. To overcome this phenomenon, using a nitrogen quenching hot casting method, lead-free tin-based quasi-2D perovskite films of PEA_2SnI_4 were formulated by Yun et al. In order to enhance the properties of the films, an additive in the form of tin fluoride (SnF_2) was incorporated during the preparation process under ambient conditions.[128] Figure 11k displays the procedure utilized for fabricating PEA_2SnI_4 films. When the SnF_2 concentration is optimized at 20%, the response speed of the PDs can achieve 0.56 ms, and the specific detectivity is an impressive 6.32×10^{13} Jones. This particular combination of tin halide perovskite-based PDs is the most remarkable one reported so far. The inclusion of SnF_2 as an additive hinders the creation of Sn vacancy and enhances the crystallinity of the PEA_2SnI_4 film. The research conducted here presents a technology for air treatment that can be easily commercialized, all while being Pb-free perovskite. Furthermore, the incorporation of SnF_2 as an engineering additive proves to be highly effective in showcasing the exceptional performance of the PDs, making them ideal for image recognition applications (Figure 11l).

The significance of additive engineering in regulating grain size and passivating defects is underscored in the context of future perovskite optoelectronic applications, as well as the attainment of exceptional performance in PDs devices. Given the auxiliary impact of additives on the process of film formation, it becomes imperative to explore additional substances with potential suitability as additives for the fabrication of superior perovskite films.

5.2. Post-Treatment Engineering

Perovskite materials possess numerous benefits, including excellent processability in solutions, extended carrier mobility, affordable raw material cost, and substantial optical absorption coefficient. These qualities position them as a highly promising contender for the photodetector field. Nonetheless, the material's significant drawback lies in its elevated defect density, which hinders its competitiveness within the realm of photoelectric devices. To surmount certain inherent and surface-related flaws, enhance device stability and durability, and maintain a competitive edge, post-manufacturing processing techniques are implemented.

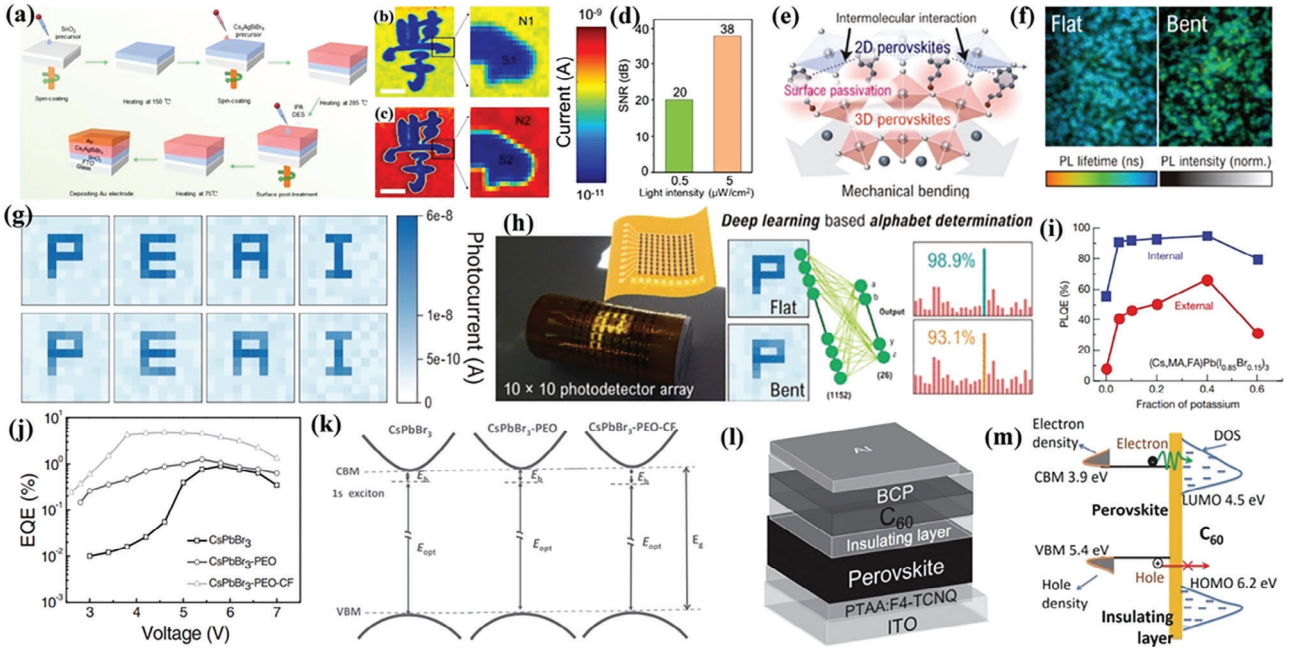

Figure 12. a) PDs preparation process and surface post-treatment diagram. b,c) The imaging results were obtained at light intensities of 0.5 and 5 μW cm^{-2}, respectively (the scale bar is 0.4 cm). d) Signal/noise ratio of the imaging results extracted from (b) and (c). a–d) Reproduced with permission.[131] Copyright 2022, Elsevier B.V. e) Schematic illustration of PEAI treatment on a pristine $FAMAPb(Br_XI_{1-X})_3$ mixed-halide structure. f) Fluorescence lifetime imaging microscopy images of flat and bent surfaces of pristine and PEAI-treated mixed-halide perovskites. The scale indicates 2 μm. g) The resulting photographs of flat (top) and mechanically bent (bottom) PEAI-treated perovskite photodetector arrays under the illumination of letters P, E, A, and I. h) Network architecture of the convolutional neural network for deep learning. e–h) Reproduced with permission.[132] Copyright 2022, American Chemical Society. i) PLQE of perovskite films passivated with various potassium fractions, measured under 532 nm laser irradiation, excitation intensity equivalent to about 1 sun (60 mW cm^{-2}). Reproduced with permission.[133] Copyright 2018, Springer. j) EQE versus voltage characteristics. k) Schematic diagram of the electronic band gap (E_g), optical band gap (E_{opt}), and exciton binding energy (E_b) of the original $CsPbBr_3$, $CsPbBr_3$-PEO, and $CsPbBr_3$-PEO-CF films. Reproduced with permission.[134] Copyright 2014, American Chemical Society. l) Structure of a device integrating a polymer insulating layer, and m) energy diagram illustrating how this insulating layer inhibits surface charge recombination. The insulation layer inhibits charge recombination by separating excess electrons and holes in the electron transport layer and in the perovskite layer. l,m) Reproduced with permission.[135] Copyright 2016, Wiley-VCH.

5.2.1. Surface Passivation Treatment

Beside implementing annealing, certain studies have suggested performing additional treatments on the perovskite film's surface in order to address certain physical (such as band misalignment between the perovskite layer and subsequent layers) or chemical (like ion migration and charged vacancy) phenomena that lead to the formation of interfacial recombination centers.[39–129,130] In this regard, Li et al. reported a lead-free $Cs_2AgBiBr_6$ perovskite PDs that improved photodetection performance by post-processing with isopropyl alcohol (IPA) solvent.[131] The schematic diagram of the preparation process of PDs, specifically $Cs_2AgBiBr_6$ PDs, is depicted in **Figure 12**a. The exceptional self-powered photoelectric detection performance of $Cs_2AgBiBr_6$ PDs can be attributed to the heterostructure construction and solvent post-treatment of the perovskite surface. Notably, this PD demonstrates a responsivity of 48 mA W^{-1}, a specific detectivity of 2.1×10^{12} Jones, a switching ratio of 9000, and response speeds of 248 μs/341 μs. Furthermore, utilizing $Cs_2AgBiBr_6$ PDs as an imaging sensor, a transmission imaging system has been successfully assembled (Figure 12b–d). According to the findings, the imaging capability of the $Cs_2AgBiBr_6$ PD-based system exhibits exceptional high resolution and contrast, especially in low light scenarios. Kim et al. conducted an experiment where they used the PEAI organic spacer to treat perovskite surfaces.[132] This treatment resulted in the formation of 2D perovskite passivation layers. The main aim of this process was to effectively regulate the trap-assisted recombination pathways by addressing the surface halide defects and inducing halide segregation through photoinduced mechanisms (Figure 12e). Furthermore, PEAI serves as a remedy for iodide vacancies on the perovskite layers' surface, which manifest as centers for non-radiative recombination. Examination of the fluorescence lifetime of planar and curved surfaces of $FAMAPb(Br_xI_{1-x})_3$ perovskite using imaging reveals the lattice's ability to withstand mechanical strain by assuaging and securing ion halide defects (Figure 12f). The flexible photodetector, after undergoing post-processing, exhibits remarkable competence in optical imaging, as displayed in Figure 12g. In this study, valuable guidance for the development of next-generation optoelectronic applications is provided by the connection revealed between the kinetics and mechanical properties of chemically modified charge carriers. The use of deep learning algorithms in combination with a flexible array of passivated perovskite has demonstrated outstanding accuracy in determining letters in both flat (>96%) and curved (>93%) states, as illustrated in Figure 12h.

Moreover, Li et al. reported the treatment of $MAPbI_3/PbI_2$ composite films with MAI in ethanol. After MAI treatment, $MAPbI_3/PbI_2$ composite film is transformed into pure $MAPbI_3$ perovskite membrane.[136] Under the white light irradiation of 0.5 mW cm^{-2}, the film achieved an ultra-high response of 3.6 A W^{-1} and a detectivity of 5.4×10^{12} Jones. The excellent photo-response performance is attributed to the improved electron quality of the treated perovskite films. t-Butyl ammonium iodide (t-BAI), propylammonium iodide (PAI, $C_3H_{10}NI$), and phenylethyl ammonium bromide (PEABr) are additional examples of ammonium salts that have proven to be effective interfacial modifiers when used with perovskite. These salts have the advantage of not reacting with the perovskite material itself. The preparation and post-treatment of these salts offer unique benefits, such as reducing the number of interfacial defects and minimizing the mismatch between the cap layer and the 3D perovskite lattice. This results in improved performance and stability of perovskite-based devices. Our group introduced PAI to post-treat the surface of $MAPbI_3$ film, which further improved the performance and stability of the film.[117] Furthermore, several recent studies have indicated that halide compounds, namely diammonium iodide, iodopentafluorobenzene, quaternary ammonium halides, and potassium halide, along with polystyrene thin insulating layers,[133,134,137,138] can be employed as post-treatments for perovskite films. These treatments effectively exploit the intermolecular interactions to passivate the suspended bonds within the perovskite layers. According to a study conducted by Abdi-Jalebi et al., the application of passivated potassium halide layers on surfaces and grain boundaries can effectively minimize non-radiative losses and photoinduced ion migration in perovskite films and interfaces.[133] It was discovered that this approach resulted in a remarkable external photoluminescence quantum yield of 66%, indicative of an internal yield exceeding 95% (Figure 12i). By maintaining a high mobility of over 40 square centimeters per volt per second, they were able to achieve a commendable luminescence rate while simultaneously ensuring excellent charge transport. This achievement represents a rare combination of exceptional luminescence and superior charge transfer capabilities. The charge accumulation and subsequent recombination losses in working solar cells due to trap states on the perovskite surface were analyzed by Abate et al.[134] Following this, the researchers successfully improved the device performance by identifying the coordination iodide ions responsible for these trap states within the perovskite structure and passivating them using supramolecular halogen bond complexation (Figure 12j,k). Wang et al. provided evidence that the insertion of a tunnel polystyrene layer between the perovskite material and the electron transport layer results in a noteworthy enhancement of the device's performance. This improvement primarily arises from the suppression of carrier recombination at the cathode contact.[135] Figure 12l displays the schematic diagram of the device structure that was utilized in their investigation. By spatially separating the photogenerated electrons and holes at the interface of the perovskite and cathode, the tunneling layer effectively diminishes charge recombination, as shown in Figure 12m. Moreover, the implementation of a hydrophobic polymer-based tunneling layer greatly fortifies the device's resistance against water-induced damage. Importantly, this approach offers simplicity as it negates the requirement for a lattice match between the buffer layer and the perovskite material.

5.2.2. Post-Treatment of Grain Boundaries

Non-radiative recombination centers are rendered highly vulnerable to environmental instability due to the buildup of defects at grain boundaries. Numerous post-processing techniques have been devised to tackle this concern, aiming at diminishing grain boundaries and hence minimize non-radiative recombination centers. Zhao et al. introduced a tandem-like perovskite PDs and suggested an enhanced solution process that utilizes excessive polymethyl methacrylate (PMMA) as an antisolvent to promote perovskite crystal growth and minimize horizontal grain boundaries.[139] **Figure 13**a,b displays the experimental procedure and the cross-sectional SEM, respectively. Moreover, the PMMA, which remains within the perovskite grains, functions as an intermediary layer to store optical carriers. This leads to a decrease in dark current and an enhancement in PDs gain. The findings demonstrate that when illuminated with a wavelength of 532 nm, the ideal perovskite PD exhibits a detectivity of 3.38 $\times 10^{12}$ Jones, a responsivity of 5.65 A W^{-1}, and a EQE of 1300% (Figure 13c).

According to Du et al., it is possible to attain high-quality films solely through annealing and grain growth processes without the need for passivation agents, by loosening the criteria for film smoothness.[140] The morphological changes resulting from the evaporation of the MACl-DMF solution have been found to effectively eliminate defects in the film. By examining the deposited film at a nanoscale level, researchers were able to visualize and identify clusters of defects. However, after treatment, these defect clusters were observed to disappear. Additionally, the film displayed emission grain boundaries and demonstrated impressive intergranular uniformity in polycrystalline films (Figure 13d–g). Xiao and colleagues presented a novel technique for post-treatment, involving the annealing of 3D perovskite $MAPbI_3$ in either *N, N*-dimethylformamide (DMF) or dimethyl sulfoxide (DMSO) vapor.[143] It turned out that the size of grains grown in an inert environment was twice larger than those grown in an inert environment, suggesting that grains grown in a vapor are much larger than those grown in an inert atmosphere. This post-processing strategy has been shown important for reducing grain boundary density and related defects. The two-step technique employed by Chen et al. involved aligning 2D perovskite for post-treatment. In this process, guanidine thiocyanate (GASCN, $C_2H_6N_4S$) and MACl were utilized as post-treatment agents (as depicted in Figure 13h).[141] Initially, GASCN was employed for the first-step post-treatment, which resulted in a considerable reduction in grain gap within the perovskite film. As a consequence, the arrangement of grains improved significantly, leading to a more orderly configuration. Subsequently, the second-step post-processing involving MACl was performed to passivate the trap state present in the perovskite film. This step was found to considerably enhance the device performance (Figure 13i). In addition, Lin et al. proposed a facile bulk recrystallization process by coating the surface of perovskite with formamidinium chloride (FACl) to remove excess PbI_2 from the crystals.[142] The schematic illustration of the FACl

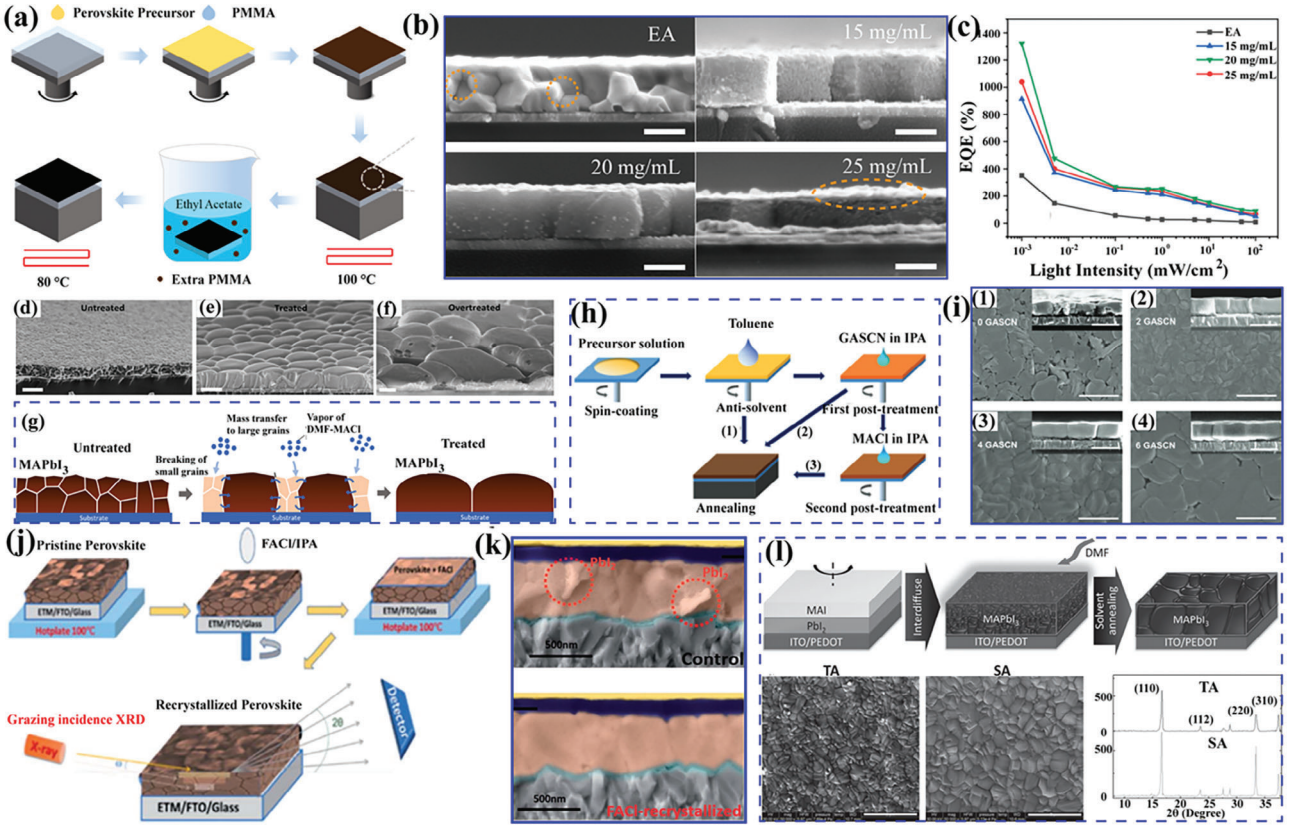

Figure 13. a) Schematic diagram of an excess polymer-assisted crystal growth method. b) Cross-sectional SEM images of the perovskite structure treated with PMMA of different concentrations: 0 mg mL^{-1}, 15 mg mL^{-1}, 20 mg mL^{-1}, and 25 mg mL^{-1}. c) EQE under different intensities of irradiation at 532 nm of $MAPbI_3$ heterojunction PD treated with different concentrations of PMMA. a–c) Reproduced with permission.[139] Copyright 2022, Elsevier B.V. d–f) SEM images of tilted cross sections of untreated $MAPbI_3$ film after anti-solvent assisted spin coating, $MAPbI_3$ film treatment for 5 min, and $MAPbI_3$ film overtreatment for 10 min. All images have a scale of 500 nm. g) Schematic diagram of $MAPbI_3$ membrane morphology transformation during MACl treatment and process of aerosol entry into $MAPbI_3$ film. Larger $MAPbI_3$ grains grow at the expense of smaller surrounding grains. d–g) Reproduced with permission.[140] Copyright 2022, American Chemical Society. h) Sequential post-fabrication process of perovskite device. i) Top view and cross section of quasi-2D perovskite films treated with different GASCN solutions (illustration). The scale in the top view is 1 µm, and the scale in the illustration is 500 nm. h,i) Reproduced with permission.[141] Copyright 2019, Wiley-VCH. j) Schematic illustration of the FACl deposition method. k) False-color SEM images depicting a cross-section of a controlled and optimized FACl recrystallized perovskite device. j,k) Reproduced with permission.[142] Copyright 2019, Royal Society of Chemistry. l) Schematic illustration of expansion of perovskite grains and reduction of grain boundaries by interprocess diffusion and antisolvent methods. Top-scan SEM micrographs and XRD of hot annealed (TA) and solvent annealed (SA) perovskite films. Reproduced with permission.[143] Copyright 2014, Wiley-VCH.

deposition method is shows in Figure 13j. Massive recrystallization was demonstrated and observed by means of grazing X-ray diffraction (XRD) analysis of the functional relationship between the crystal structure and the depth profile and SEM (Figure 13k). The reconstructed crystal shows better photoelectric quality, reduced interface recombination, and enhanced device stability. In this study, both solvent and antisolvent post-treatment methods are found to promote the growth of large grains (Figure 13l). However, the underlying principles behind this phenomenon are not yet well understood.[143] The authors suggest that the compounds used in the post-treatment process may contribute to the migration of grain boundaries in perovskite by forming intermediates. This observation provides a plausible explanation for the enhanced grain growth, but further research is needed to fully elucidate the mechanisms involved.[144]

In summary, surface passivation is advantageous for preventing external degradation of perovskite optoelectronic devices by creating a barrier between the absorber and stressors such as water or molecular oxygen. This improves device stability. However, adding a capping layer can hinder charge extraction and lead to large photocurrent hysteresis. On the other hand, grain boundary passivation is more effective in mitigating internal instability factors like ion migration and interface defects. However, it alone cannot improve device stability as it does not address environmental factors. Therefore, selecting a post-processing strategy should depend on the device structure and target defects for mitigation.

6. Conclusions and Outlook

Organic–inorganic hybrid 3D perovskites have been extensively explored as new photoelectric materials, due to their high light absorption coefficient, long exciton diffusion length, low manufacturing cost, and easy large-scale production. The excellent

Table 1. Comparison of the characteristic parameters of 3D perovskite-based PDs.

Device structure	R [A W^{-1}] (Bias, wavelength, irradiance)	D^* [Jones]	Rising/falling times	On/off	Wavelength	Stability time test[a)]	Ref.
(Vertical)	0.37 (0 V, 685 nm, —)	1.06×10^{12}	5.02/	—	350–750 nm	>3000 s	[59]
Ag/BCP/PCBM/$MAPbI_3$:CuSCN/ITO			5.50 µs				
(Vertical)	0.046 (0.7 V, 710 nm, 0.01 W cm^{-2})	1.75×10^{10}	—	7.8×10^7	300–800 nm	—	[56]
Ag/P3HT/$MAPbI_3$							
/PCBM/TiO_2/$MAPbBr_3$/P3HT/NiO_x/ITO							
(Vertical)	0.314 (0 V, 670 nm, 1 mW cm^{-2})	—	4.0/3.3 µs	10^4	400–750 nm	—	[145]
Au/PEDOT:PSS/							
$MAPbI_3$ film/PCBM/Al							
(Lateral)	0.1 (10 V, 650 nm, 100 µW cm^{-2})	1.02×10^{12}	0.3/	300	<800 nm	4 weeks	[146]
Au/$MAPbI_3$ arrays/Au			0.4 ms				
(Vertical)	0.21 (−2 V, white light, 143 µW cm^{-2})	7.4×10^{12}	120 ns	—	<800 nm	45 days	[147]
Al/BCP/C60/PCBM							
/$MAPbI_3$ Poly							
/PEDOT:PSS/ITO							
(Vertical)	—	7.13×10^{11}	—	—	600–900 nm	>120 h	[148]
Au/PTAA/$MAPbI_3$/Au nanosquares/Au							
(Lateral)	24.8 (10 V, 532 nm, 0.37 mW cm^{-2})	7.7×10^{12}	4.0/	2.4×10^4	300–850 nm	>20 days	[149]
Au/C8BTBT-$MAPbI_3$/Au			5.8 ms				
(Lateral)	0.018 (−2 V, 970 nm, 0.05 mW cm^{-2})	1.8×10^{12}	—	298	400–1200 nm	—	[29]
Si/SiO2/Au/$MAPbI_3$/Au/SiO_2/Si							
(Lateral)	3.27 (9 V, 645 nm, 18 nW)	1.35×10^{12}	0.3	—	<815 nm	>1400 s	[90]
$FAPbI_3$/Au/SiO_2/Si			/0.5 ms				
(Vertical)	0.53 (−0.1 V, 900 nm, —)	2.07×10^{11}	35 ns	—	300–1050 nm	>280 h	[150]
ITO/PTAA/PEAI/$Cs_{0.05}MA_{0.45}FA_{0.50}Pb_{0.5}Sn_{0.5}I_3$/$C_{60}$/BCP/Cu							

[a)] Stability tests are based on different test conditions.

photoelectric characteristics of hybrid halide perovskites have rendered them desirable for optical communication, optical imaging, image sensing, environmental monitoring, and optical interconnection applications. Nonetheless, the lack of environmental stability poses a hindrance to the industrialization of 3D perovskite devices. Halide 2D/quasi-2D perovskites offer good environmental stability, making them a promising option for the design and development of high-stability perovskite optoelectronic devices. The comparison between traditional 3D perovskite-based devices and quasi-2D perovskite-based devices in terms of photoelectric performance is essential. We have gathered in **Tables 1** and **2** the main systems and performances reported in the literature for the two categories, respectively. However, it should be emphasized that the latter still falls short in terms of its ability to absorb light and efficiently transport carriers, mainly due to its insufficient crystal growth orientation, phase distribution, and large band gap. We have also mentioned that for photodetectors based on 2D/quasi-2D perovskite, the orientation of the quantum wells of the perovskite impacts the choice of the final PD structure. Hence, when the orientation of quantum wells of a 2D/quasi-2D perovskite is aligned perpendicular to the substrate, as in Figures 1a and 11b, it is better suited for vertical PDs. Conversely, the quantum wells parallel to the substrate are more suited to lateral PDs (Figure 1b,c).

Although the perovskite semiconductors' integration into high-resolution imaging and high-speed optical communication systems holds potential advantages, the procedure is still quite difficult. Nevertheless, the manufacturing process of solution-processed perovskite semiconductors provides a feasible solution for compact photoelectric devices because of their

Table 2. Comparison of the characteristic parameters of 2D/quasi-2D perovskite-based PDs.

Device structure	R [A W^{-1}] (Bias, wavelength, irradiance)	D^* [Jones]	Rising/falling times	On/off	Wavelength	Stability time test[a)]	Ref.
(Lateral)	1.46 (0 V, 265 nm, 0.005 mW cm^{-2})	9.4×10^{12}	3.4/	10^4	265 nm	>100 days	[67]
Ag/$Cs_2AgBiBr_6$/Ag			8.4 ms				
(Lateral)	0.95(10 V, 475 nm, 8 mW cm^{-2})	3×10^{11}	310/520 µs	10^3	365–650 nm	>60 days	[151]
Ag/$(HFA)_2FAPb_2I_7$/Ag							
(Lateral)	0.4 (1.5 V, 532 nm, 1 mW cm^{-2})	1.68×10^{12}	43/	10^2	532 nm	>9 days	[81]
Au/$(iBA)_2(MA)_3Pb_4I_{13}$/Au			22 ms				
(Lateral)	0.121 (0 V, 700 nm, 5.46 nW cm^{-2})	8.09×10^9	34/	500	400–800 nm	>1000 s	[152]
Graphene/ MoS_2/$(PEA)_2SnI_4$/MoS_2/ Graphene			38 ms				
(Lateral)	5.48 (2 V, 405 nm, 0.27 µW cm^{-2})	8.2×10^{12}	12.8/10.1 µs	2×10^4	405–808 nm	>100 days	[19]
ITO/Au/$(BA)_2FAPb_2I_7$/Au/ITO							
(Lateral)	4.7 (2 V, 405 nm, 0.27 µW cm^{-2})	6.3×10^{12}	—	5×10^3	405–808 nm	>40 days	[21]
ITO/Au/$(PMA)_2FAPb_2I_7$ /Au/ITO							
(Lateral)	2.3 (2 V, 400 nm, 0.25 µW cm^{-2})	3.2×10^{12}	9.74/8.91 µs	—	400–1100 nm	>1000 h	[61]
Au/PEDOT:PSS-$(BA)_2FAPb_2I_7$-C8BTBT/Au							
Gate:Au/SiO_2							

[a)] Stability tests are based on different test conditions.

uncomplicated manufacturing process, adaptable chemical structure, and diverse device configurations. Unfortunately, solution treated perovskite polycrystalline films can have grain boundary defects, which hinder carrier transport and lead to poor charge mobility. To improve the photoelectric capabilities of PDs, it is crucial to fabricate a long-lasting and superior perovskite film, which serves as the optical absorption layer. To achieve this, the perovskite film should have a favorable surface/interface morphology, preferred lateral crystal growth direction, and a well-balanced phase composition and distribution.

In this review, we first introduced that perovskite film PDs have good application prospects in optical communication and imaging. Perovskite films prepared using simple solution treatment methods are typically categorized as either 3D perovskite films or 2D/quasi-2D perovskite films. Currently, research is focused on 3D perovskite PDs due to their exceptional photoelectric performance, although their stability remains a concern. On the other hand, 2D/quasi-2D perovskite films offer good environmental stability, providing new opportunities for the design and development of high stability optoelectronic devices. However, their photoelectric performance is not as strong as that of 3D perovskite films. Therefore, both perovskite films have advantages and disadvantages in their application in PDs. We have compiled methods and strategies to enhance the crystallinity, reduce surface defects, and increase the environmental stability of 3D and 2D/quasi-2D perovskite films, ultimately improving the photoelectric performance of their photodetectors. These improvements make them more suitable for optical communication and imaging applications. The various preparation strategies available offer promising opportunities for the production of superior perovskite films, which is a crucial step in the study of material and device properties. To enhance the performance of perovskite photodetectors (PDs), preparation strategies can be categorized into component engineering, interface engineering, heterojunction engineering, and film crystallinity engineering. Among these strategies, the solution treatment of perovskite film stands out as it can effectively reduce surface and structural defects, optimize crystallinity, and significantly improve device performance. Here, we specifically investigated strategies to enhance the crystallinity of perovskite films, including additive engineering and post-treatment engineering. The solution processing strategy simplifies the preparation process and effectively reduces the growth rate of perovskite, resulting in improved film quality with fewer pinholes and large size grains. This approach facilitates the production of high-quality films. Additionally, the film can be passivated more efficiently through additive and post-treatment engineering, reducing the defect state density of the film, achieving preferred orientation, and increasing grain size. As a result, carrier mobility and photoelectric conversion efficiency are significantly improved. This advancement in technology has resulted in photodetectors (PDs) with superior performance, fast response speed, and excellent environmental stability. These improvements allow for better integration of PDs into

high-resolution imaging and high-speed optical communication systems.

Prior to suggesting strategies to improve the quality of perovskite film formation, it is crucial to understand the factors that influence the film formation process and ultimately determine the film quality. Many research papers on perovskite optoelectronic devices have identified three main factors that affect film quality: internal factors, external factors, and interface regulation. Internal factors pertain to the molecular composition of the perovskite and how it impacts film quality. External factors, on the other hand, are adjustable factors involved in the manufacturing processes. Based on the dependency of film quality on preparation technology, the solution spin coating method offers a viable alternative for large-scale production of high-quality perovskite films. In this paper, the proposed strategies mainly focus on the spin-coating method for solution treatment. However, upon closer examination, it is evident that both additive engineering and post-treatment engineering offer greater adaptability and reproducibility in improving the film quality. Therefore, by optimizing the compatibility in equipment configuration with the perovskite precursor solution and phase distribution, high-quality perovskite films can be prepared.

This study highlights optimization strategies for improving perovskite photodevices. However, the current stability and photoelectric performance of perovskite-based photodetectors lag behind industrial production demands. As a result, we have compiled key recommendations to accelerate the commercial development of perovskite photodetectors in the future:

1) Although optoelectronic devices based on 3D perovskites demonstrate impressive photoelectric capabilities, their stability remains a concern and susceptibility to environmental conditions can lead to structural integrity issues. These challenges pose significant obstacles to their viability for widespread industrial implementation. However, the development and optimization of different types of perovskites has led to the creation of 2D/quasi-2D layered metal halide perovskites, which have demonstrated excellent photoelectric adjustability and environmental stability. These properties make them a promising replacement for 3D perovskites. The introduction of organic spacer cations can be used to modify halogen perovskite materials and create low-dimensional structures. This approach has two benefits: first, it can improve the stability of perovskite materials, which is important for device performance. Second, reducing the dimensionality of perovskite materials can alter the properties of its internal excitons and lead to unique photoelectric properties. These properties make them promising materials for use in PDs.
2) 2D/quasi-2D perovskite undergoes the disruption of its regular metal framework while incorporating defects of electron donors and hole acceptors possessing lower energy levels. As a consequence, the diffusion length and mobility of the charge carriers in 2D/quasi-2D perovskite are diminished. To improve the photoelectric performance of perovskite PDs, additive engineering and post-treatment engineering are effective treatment methods. Through facile solution treatment methods, suitable additives can be introduced to reduce defects and grain boundaries in perovskite films and improve crystallinity. The post-processing method can enhance the quality of the film surface, facilitate the growth of the vertically (or laterally) aligned quantum well structure, and ultimately improve the photoelectric performance of the vertical (or lateral) structure device.
3) In the realm of synthetic methods, while metal halide perovskite is recognized for its easy preparation and diverse morphology, it is imperative to delve deeper into the growth dynamics to produce top-notch perovskite films. Specifically, it is crucial to investigate how additives can minimize surface and structural defects of thin films, and how post-processing can facilitate oriented growth of quantum wells in quasi-2D perovskite, thereby enhancing smooth carrier transport and promoting oriented growth.
4) The challenge lies in integrating perovskite photodetectors into high-resolution imaging and high-speed optical communication systems. This difficulty arises from the incompatibility between perovskite materials and conventional lithography techniques, as well as in stripping with polar solutions. Miniaturizing and integrating perovskite devices while ensuring their photoelectric performance is challenging.
5) As the exploration of halide perovskites advance, their benefits in the field of photoelectric devices are becoming more apparent. Researchers have made significant progresses by inventing a range of photodetectors utilizing quasi-2D perovskite substances in order to fulfill the diverse demands of various devices. Nevertheless, further enhancements and refinements are still needed at this early stage of the research. It is crucial for the size, performance, and stability of the devices to align with practical requirements to ensure its usability and competitiveness. Hence, theoretical and experimental investigation of the stability of a photodetector that relies on a novel quasi-2D layered perovskite material and its perovskite heterojunction is profoundly important.

Conflict of Interest

The authors declare no conflict of interest.

Keywords

halide perovskite, material dimension, optical communication, optical imaging, photodetector

Received: September 15, 2023
Revised: November 11, 2023
Published online:

[1] S. Chen, C. Teng, M. Zhang, Y. Li, D. Xie, G. Shi, *Adv. Mater.* **2016**, *28*, 5969.
[2] F. Cao, T. Yan, Z. Li, L. Wu, X. Fang, *Adv. Opt. Mater.* **2022**, *10*, 2200786.
[3] J. Feng, C. Gong, H. Gao, W. Wen, Y. Gong, X. Jiang, B. Zhang, Y. Wu, Y. Wu, H. Fu, L. Jiang, X. Zhang, *Nat. Electron.* **2018**, *1*, 404.
[4] X. Hu, X. Zhang, L. Liang, J. Bao, S. Li, W. Yang, Y. Xie, *Adv. Funct. Mater.* **2014**, *24*, 7373.
[5] R. F. Oulton, V. J. Sorger, T. Zentgraf, R.-M. Ma, C. Gladden, L. Dai, G. Bartal, X. Zhang, *Nature* **2009**, *461*, 629.

[6] F. Feng, G. Si, C. Min, X. Yuan, M. Somekh, *Light: Sci. Appl.* **2020**, *9*, 95.
[7] Z. Wang, Z. Dong, H. Zhu, L. Jin, M.-H. Chiu, L.-J. Li, Q.-H. Xu, G. Eda, S. A. Maier, A. T. S. Wee, C.-W. Qiu, J. K. W. Yang, *ACS Nano* **2018**, *12*, 1859.
[8] W. Liang, Z. Xiao, H. Xu, H. Deng, H. Li, W. Chen, Z. Liu, Y. Long, *Opt. Express* **2020**, *28*, 31330.
[9] T. Yu, F. Wang, Y. Xu, L. Ma, X. Pi, D. Yang, *Adv. Mater.* **2016**, *28*, 4912.
[10] X. Li, Z. Deng, J. Li, Y. Li, L. Guo, Y. Jiang, Z. Ma, L. Wang, C. Du, Y. Wang, Q. Meng, H. Jia, W. Wang, W. Liu, H. Chen, *Photonics Res.* **2020**, *8*, 1662.
[11] L. Shi, S. Nihtianov, *IEEE Sens. J.* **2012**, *12*, 2453.
[12] K.-T. Lin, H.-L. Chen, Y.-S. Lai, C.-C. Yu, *Nat. Commun.* **2014**, *5*, 3288.
[13] D. Xiong, W. Deng, G. Tian, Y. Gao, X. Chu, C. Yan, L. Jin, Y. Su, W. Yan, W. Yang, *Nanoscale* **2019**, *11*, 3021.
[14] Y. Lu, Y. Wang, C. Xu, C. Xie, W. Li, J. Ding, W. Zhou, Z. Qin, X. Shen, L.-B. Luo, *Nanoscale* **2021**, *13*, 7606.
[15] A. Kojima, K. Teshima, Y. Shirai, T. Miyasaka, *J. Am. Chem. Soc.* **2009**, *131*, 6050.
[16] Y. Zhao, F. Ma, Z. Qu, S. Yu, T. Shen, H.-X. Deng, X. Chu, X. Peng, Y. Yuan, X. Zhang, J. You, *Science* **2022**, *377*, 531.
[17] J. Park, J. Kim, H.-S. Yun, M. J. Paik, E. Noh, H. J. Mun, M. G. Kim, T. J. Shin, S. I. l. Seok, *Nature* **2023**, *616*, 724.
[18] K. Akihiro, Y. Shirai, M. Tsutomu, *J. Am. Chem. Soc.* **2009**, *131*, 6050.
[19] T. Wang, D. Zheng, K. Vegso, N. Mrkyvkova, P. Siffalovic, X. Yuan, M. G. Somekh, L. Coolen, T. Pauporte, F. Fu, *Nano Energy* **2023**, *116*, 108827.
[20] L. Cao, X. Liu, Y. Li, X. Li, L. Du, S. Chen, S. Zhao, C. Wang, *Front. Phys.* **2020**, *16*, 33201.
[21] T. Wang, D. Zheng, K. Vegso, N. Mrkyvkova, P. Siffalovic, T. Pauporté, *Adv. Funct. Mater.* **2023**, *33*, 2304659.
[22] L. Cheng, Z. Liu, S. Li, Y. Zhai, X. Wang, Z. Qiao, Q. Xu, K. Meng, Z. Zhu, G. Chen, *Angew. Chem., Int. Ed.* **2021**, *60*, 856.
[23] J. Jang, Y.-G. Park, E. Cha, S. Ji, H. Hwang, G. G. Kim, J. Jin, J.-U. Park, *Adv. Mater.* **2021**, *33*, 2101093.
[24] J. Wang, S. Xiao, W. Qian, K. Zhang, J. Yu, X. Xu, G. Wang, S. Zheng, S. Yang, *Adv. Mater.* **2021**, *33*, 2005557.
[25] B. Wang, C. Zhang, B. Zeng, C.-Y. Wu, C. Xie, Di Wu, Y.-X. Zhou, L.-B. Luo, *J. Phys. Chem. Lett.* **2021**, *12*, 2930.
[26] J. Wang, S. Luo, Y. Lin, Y. Chen, Y. Deng, Z. Li, K. Meng, G. Chen, T. Huang, S. Xiao, H. Huang, C. Zhou, L. Ding, J. He, J. Huang, Y. Yuan, *Nat. Commun.* **2020**, *11*, 582.
[27] X. Xu, Z. Li, L. Zhu, H. Zheng, G. Liu, T. Hayat, A. Alsaedi, X. Zhang, Y. Huang, X. Pan, *J. Mater. Chem. A* **2019**, *7*, 1341.
[28] X. Zhang, C. Ji, X. Liu, S. Wang, L. Li, Y. Peng, Y. Yao, M. Hong, J. Luo, *Adv. Opt. Mater.* **2020**, *8*, 2000311.
[29] Z. Zhang, C. Xu, C. Zhu, X. Tong, C. Fu, J. Wang, Y. Cheng, L. Luo, *Sens. Actuators, A* **2021**, *332*, 113176.
[30] J. Jeong, M. Kim, J. Seo, H. Lu, P. Ahlawat, A. Mishra, Y. Yang, M. A. Hope, F. T. Eickemeyer, M. Kim, Y. J. Yoon, I. W. Choi, B. P. Darwich, S. J. Choi, Y. Jo, J. H. Lee, B. Walker, S. M. Zakeeruddin, L. Emsley, U. Rothlisberger, A. Hagfeldt, D. S. Kim, M. Grätzel, J. Y. Kim, *Nature* **2021**, *592*, 381.
[31] Y. Liu, S. Akin, A. Hinderhofer, F. T. Eickemeyer, H. Zhu, J. Y. Seo, J. Zhang, F. Schreiber, H. Zhang, S. M. Zakeeruddin, *Angew. Chem., Int. Ed.* **2020**, *59*, 15688.
[32] Y. Du, Q. Tian, X. Chang, J. Fang, X. Gu, X. He, X. Ren, K. Zhao, S. F. Liu, *Adv. Mater.* **2022**, *34*, 2106750.
[33] S. Ahmad, P. Fu, S. Yu, Q. Yang, X. Liu, X. Wang, X. Wang, X. Guo, C. Li, *Joule* **2019**, *3*, 794.
[34] R. K. Ulaganathan, R. C. Murugesan, C. Y. Lin, A. Subramanian, W. L. Chen, Y. M. Chang, A. Rozhin, R. Sankar, *Adv. Funct. Mater.* **2021**, *32*, 2112277.
[35] S. Hu, X. Yang, B. Yang, Y. Zhang, H. Li, C. Sheng, *J. Phys. Chem. C* **2021**, *125*, 2212.
[36] J. Lu, T. Yang, T. Niu, N. Bu, Y. Zhang, S. Wang, J. Fang, X. Chang, T. Luo, J. Wen, Y. Yang, Z. Ding, K. Zhao, S. Liu, *Energy Environ. Sci.* **2022**, *15*, 1144.
[37] C. Fu, Z. Gu, Y. Tang, Q. Xiao, S. Zhang, Y. Zhang, Y. Song, *Angew. Chem., Int. Ed.* **2022**, *61*, 202117067.
[38] J. Qiu, Y. Xia, Y. Zheng, W. Hui, H. Gu, W. Yuan, H. Yu, L. Chao, T. Niu, Y. Yang, X. Gao, Y. Chen, W. Huang, *ACS Energy Lett.* **2019**, *4*, 1513.
[39] Y. Bai, S. Xiao, C. Hu, T. Zhang, X. Meng, H. Lin, Y. Yang, S. Yang, *Adv. Energy Mater.* **2017**, *7*, 1701038.
[40] J. Byun, H. Cho, C. Wolf, Mi Jang, A. Sadhanala, R. H. Friend, H. Yang, T.-W. Lee, *Adv. Mater.* **2016**, *28*, 7515.
[41] Y. Chen, S. Tan, N. Zhou, N. Yang, W. Zhou, Y. Wu, K. Weber, Q. Chen, H. Zhou, *Sol. RRL* **2019**, *3*, 1900083.
[42] R. Dong, C. Lan, X. Xu, X. Liang, X. Hu, D. Li, Z. Zhou, L. Shu, S. Yip, C. Li, S.-W. Tsang, J. C. Ho, *ACS Appl. Mater. Interfaces* **2018**, *10*, 19019.
[43] X. Li, J. M. Hoffman, M. G. Kanatzidis, *Chem. Rev.* **2021**, *121*, 2230.
[44] P. Liu, N. Han, W. Wang, R. Ran, W. Zhou, Z. Shao, *Adv. Mater.* **2021**, *33*, 2002582.
[45] N. Li, S. Apergi, C. C. S. Chan, Y. Jia, F. Xie, Q. Liang, G. Li, K. S. Wong, G. Brocks, S. Tao, N. Zhao, *Adv. Mater.* **2022**, *34*, 2202042.
[46] D. Wang, G. Li, *Laser Photonics Rev.* **2022**, *16*, 2100713.
[47] Z. Li, E. Hong, X. Zhang, M. Deng, X. Fang, *J. Phys. Chem. Lett.* **2022**, *13*, 1215.
[48] L. Mei, R. Huang, C. Shen, J. Hu, P. Wang, Z. Xu, Z. Huang, L. Zhu, *Adv. Opt. Mater.* **2022**, *10*, 2102656.
[49] H.-P. Wang, S. Li, X. Liu, Z. Shi, X. Fang, J.-H. He, *Adv. Mater.* **2021**, *33*, 2003309.
[50] L. Li, S. Ye, J. Qu, F. Zhou, J. Song, G. Shen, *Small* **2021**, *17*, 2005606.
[51] W. Wu, H. Lu, X. Han, C. Wang, Z. Xu, S.-T. Han, C. Pan, *Small Methods* **2023**, *7*, 2201499.
[52] S. Lim, M. Ha, Y. Lee, H. Ko, *Adv. Opt. Mater.* **2018**, *6*, 1800615.
[53] D. B. Mitzi, C. D. Dimitrakopoulos, L. L. Kosbar, *Chem. Mater.* **2001**, *13*, 3728.
[54] S. M. Park, A. Abtahi, A. M. Boehm, K. R. Graham, *ACS Energy Lett.* **2020**, *5*, 799.
[55] C. Bao, J. Yang, S. Bai, W. Xu, Z. Yan, Q. Xu, J. Liu, W. Zhang, F. Gao, *Adv. Mater.* **2018**, *30*, 1803422.
[56] B. Huang, J. Liu, Z. Han, Yu Gu, D. Yu, X. Xu, Y. Zou, *ACS Appl. Mater. Interfaces* **2020**, *12*, 48765.
[57] N. Ma, J. Jiang, Y. Zhao, L. He, Y. Ma, H. Wang, L. Zhang, C. Shan, L. Shen, W. Hu, *Nano Energy* **2021**, *86*, 106113.
[58] X. Pan, J. Zhang, H. Zhou, R. Liu, D. Wu, R. Wang, L. Shen, L. Tao, J. Zhang, H. Wang, *Nanomicro Lett.* **2021**, *13*, 70.
[59] Z. Liu, X. Liu, Bo Sun, X. Tan, H. Ye, J. Zhou, Z. Tang, T. Shi, G. Liao, *Adv. Mater.* **2020**, *5*, 2000260.
[60] C. H. Kang, I. Dursun, G. Liu, L. Sinatra, X. Sun, M. Kong, J. Pan, P. Maity, E.-N. Ooi, T. K. Ng, O. F. Mohammed, O. M. Bakr, B. S. Ooi, *Light: Sci. Appl.* **2019**, *8*, 94.
[61] T. Wang, D. Zheng, J. Zhang, J. Qiao, C. Min, X. Yuan, M. Somekh, F. Feng, *Adv. Funct. Mater.* **2022**, *32*, 2208694.
[62] W.-L. Tsai, C.-Y. Chen, Y.-T. Wen, L. Yang, Y.-L. Cheng, H.-W. Lin, *Adv. Mater.* **2019**, *31*, 1900231.
[63] A. Sobhani, M. W. Knight, Y. Wang, B. Zheng, N. S. King, L. V. Brown, Z. Fang, P. Nordlander, N. J. Halas, *Nat. Commun.* **2013**, *4*, 1643.
[64] W. Wu, X. Han, J. Li, X. Wang, Y. Zhang, Z. Huo, Q. Chen, X. Sun, Z. Xu, Y. Tan, C. Pan, A. Pan, *Adv. Mater.* **2021**, *33*, 2006006.
[65] J.-Y. Zhang, J.-L. Xu, T. Chen, X. Gao, S.-D. Wang, *ACS Appl. Mater. Interfaces* **2019**, *11*, 44430.
[66] Q. Wang, G. Zhang, H. Zhang, Y. Duan, Z. Yin, Y. Huang, *Adv. Funct. Mater.* **2021**, *31*, 2100857.

[67] Y. Li, Z. Shi, L. Lei, S. Li, D. Yang, D. Wu, T. Xu, Y. Tian, Y. Lu, Ye Wang, L. Zhang, X. Li, Y. Zhang, G. Du, C. Shan, *Adv. Mater. Interfaces* **2019**, *6*, 1900188.
[68] H. Wang, D. H. Kim, *Chem. Soc. Rev.* **2017**, *46*, 5204.
[69] T. Leijtens, K. A. Bush, R. Prasanna, M. D. Mcgehee, *Nat. Energy* **2018**, *3*, 828.
[70] A. Buin, P. Pietsch, J. Xu, O. Voznyy, A. H. Ip, R. Comin, E. H. Sargent, *Nano Lett.* **2014**, *14*, 6281.
[71] Z. Ma, Y. Zhang, T. Li, X. Tang, H. Zhao, J. Li, C. Ma, J. Yao, *Appl. Phys. A: Mater. Sci. Process.* **2020**, *126*, 869.
[72] W. Wu, X. Wang, X. Han, Z. Yang, G. Gao, Y. Zhang, J. Hu, Y. Tan, A. Pan, C. Pan, *Adv. Mater.* **2019**, *31*, 1805913.
[73] J. Xue, Z. Zhu, X. Xu, Y. Gu, S. Wang, L. Xu, Y. Zou, J. Song, H. Zeng, Q. Chen, *Nano Lett.* **2018**, *18*, 7628.
[74] L. Dou, Y. Yang, J. You, Z. Hong, W.-H. Chang, G. Li, Y. Yang, *Nat. Commun.* **2014**, *5*, 5404.
[75] B. Xia, M. Tu, B. Pradhan, F. Ceyssens, M. L. Tietze, V. Rubio-Giménez, N. Wauteraerts, Y. Gao, M. Kraft, J. A. Steele, E. Debroye, J. Hofkens, R. Ameloot, *Adv. Eng. Mater.* **2021**, *24*, 2100930.
[76] H. Xia, S. Tong, C. Zhang, C. Wang, J. Sun, J. He, J. Zhang, Y. Gao, J. Yang, *Appl. Phys. Lett.* **2018**, *112*, 233301.
[77] K. Yao, X. Wang, Y.-X. Xu, F. Li, L. Zhou, *Chem. Mater.* **2016**, *28*, 3131.
[78] G. Cen, Y. Liu, C. Zhao, G. Wang, Y. Fu, G. Yan, Y. Yuan, C. Su, Z. Zhao, W. Mai, *Small* **2019**, *15*, 1902135.
[79] H. L. Zhu, H. Lin, Z. Song, Z. Wang, F. Ye, H. Zhang, W.-J. Yin, Y. Yan, W. C. H. Choy, *ACS Nano* **2019**, *13*, 11800.
[80] H. Li, X. Shan, J. N. Neu, T. Geske, M. Davis, P. Mao, K. Xiao, T. Siegrist, Z. Yu, *J. Mater. Chem. C* **2018**, *6*, 11961.
[81] R. Dong, C. Lan, F. Li, S. Yip, J. C. Ho, *Nanoscale Horiz.* **2019**, *4*, 1342.
[82] H.-D. Lee, H. Kim, H. Cho, W. Cha, Y. Hong, Y.-H. Kim, A. Sadhanala, V. Venugopalan, J. S. Kim, J. W. Choi, C.-L. Lee, D. Kim, H. Yang, R. H. Friend, T.-W. Lee, *Adv. Funct. Mater.* **2019**, *29*, 1901225.
[83] F. Zhang, H. Lu, J. Tong, J. J. Berry, M. C. Beard, K. Zhu, *Energy Environ. Sci.* **2020**, *13*, 1154.
[84] L. N. Quan, M. Yuan, R. Comin, O. Voznyy, E. M. Beauregard, S. Hoogland, A. Buin, A. R. Kirmani, K. Zhao, A. Amassian, D. H. Kim, E. H. Sargent, *J. Am. Chem. Soc.* **2016**, *138*, 2649.
[85] N. R. Venkatesan, J. G. Labram, M. L. Chabinyc, *ACS Energy Lett.* **2018**, *3*, 380.
[86] Y. Xie, H. Yu, J. Duan, L. Xu, B. Hu, *ACS Appl. Mater. Interfaces* **2020**, *12*, 11190.
[87] S. Han, Y. Yao, X. Liu, B. Li, C. Ji, Z. Sun, M. Hong, J. Luo, *Small* **2019**, *15*, 1901194.
[88] D. Sirbu, F. H. Balogun, R. L. Milot, P. Docampo, *Adv. Energy Mater.* **2021**, *11*, 2003877.
[89] D. B. Mitzi, K. Chondroudis, C. R. Kagan, *IBM J. Res. Dev.* **2001**, *45*, 29.
[90] D. Yu, F. Cao, Y. Gu, Z. Han, J. Liu, B. Huang, X. Xu, H. Zeng, *Nano Res.* **2020**, *14*, 1210.
[91] X. Huang, Q. Li, W. Shi, K. Liu, Y. Zhang, Y. Liu, X. Wei, Z. Zhao, Y. Guo, Y. Liu, *Small* **2021**, *17*, 2102820.
[92] J. Gong, P. Guo, S. E. Benjamin, P. G Van Patten, R. D. Schaller, T. Xu, *J. Energy Chem.* **2018**, *27*, 1017.
[93] W. Kong, C. Zhao, T. Huang, X. Li, J. Xing, Z. Yu, P. Yang, W. Li, W. Yu, *ACS Appl. Mater. Interfaces* **2022**, *14*, 28154.
[94] Y. Wang, X. Zhang, D. Wang, X. Li, J. Meng, J. You, Z. Yin, J. Wu, *ACS Appl. Mater. Interfaces* **2019**, *11*, 28005.
[95] W. Rehman, D. P. Mcmeekin, J. B. Patel, R. L. Milot, M. B. Johnston, H. J. Snaith, L. M. Herz, *Environ. Sci.* **2017**, *10*, 361.
[96] J. Shi, Y. Gao, X. Gao, Y. Zhang, J. Zhang, X. Jing, M. Shao, *Adv. Mater.* **2019**, *31*, 1901673.
[97] Y. Wang, X. Zhang, Q. Jiang, H. Liu, D. Wang, J. Meng, J. You, Z. Yin, *ACS Appl. Mater. Interfaces* **2018**, *10*, 6505.
[98] S. Demchyshyn, M. Verdi, L. Basiricò, A. Ciavatti, B. Hailegnaw, D. Cavalcoli, M. C. Scharber, N. S. Sariciftci, M. Kaltenbrunner, B. Fraboni, *Adv. Sci.* **2020**, *7*, 2002586.
[99] H. Mescher, F. Schackmar, H. Eggers, T. Abzieher, M. Zuber, E. Hamann, T. Baumbach, B. S. Richards, G. Hernandez-Sosa, U. W. Paetzold, U. Lemmer, *ACS Appl. Mater. Interfaces* **2020**, *12*, 15774.
[100] D. Yu, F. Cao, Y. Shen, X. Liu, Y. Zhu, H. Zeng, *J. Phys. Chem. Lett.* **2017**, *8*, 2565.
[101] T. Zhu, J. Su, J. Alvarez, G. Lefèvre, F. Labat, I. Ciofini, T. Pauporté, *Adv. Funct. Mater.* **2019**, *29*, 1903981.
[102] K. Xia, W. Wu, M. Zhu, X. Shen, Z. Yin, H. Wang, S. Li, M. Zhang, H. Wang, H. Lu, A. Pan, C. Pan, Y. Zhang, *Sci. Bull.* **2020**, *65*, 343.
[103] L.-H. Zeng, Q.-M. Chen, Z.-X. Zhang, D. Wu, H. Yuan, Y.-Y. Li, W. Qarony, S. P. Lau, L.-B. Luo, Y. H. Tsang, *Adv. Sci.* **2019**, *6*, 1901134.
[104] G. Yan, Z. Ji, Z. Li, B. Jiang, M. Kuang, X. Cai, Y. Yuan, W. Mai, *Sci. China Mater.* **2020**, *64*, 198.
[105] F. Feng, T. Wang, J. Qiao, C. Min, X. Yuan, M. Somekh, *ACS Appl. Mater. Interfaces* **2021**, *13*, 61496.
[106] Q. Wang, Qi Zhang, X. Luo, J. Wang, R. Zhu, Q. Liang, L. Zhang, J. Z. Yong, C. P. Yu Wong, G. Eda, J. H. Smet, A. T. S. Wee, *ACS Appl. Mater. Interfaces* **2020**, *12*, 45235.
[107] C. Li, J. Lu, Y. Zhao, L. Sun, G. Wang, Y. Ma, S. Zhang, J. Zhou, L. Shen, W. Huang, *Small* **2019**, *15*, 1903599.
[108] T. Zhu, J. Su, F. Labat, I. Ciofini, T. Pauporté, *ACS Appl. Mater. Interfaces* **2020**, *12*, 744.
[109] J. Su, T. Zhu, T. Pauporté, I. Ciofini, F. Labat, *J. Comput. Chem.* **2020**, *41*, 1740.
[110] T. Zhu, D. Zheng, J. Liu, L. Coolen, T. Pauporté, *ACS Appl. Mater. Interfaces* **2020**, *12*, 37197.
[111] J. Li, G. Zhang, Z. Zhang, J. Li, Z. Uddin, Y. Zheng, Y. Shao, Y. Yuan, B. Yang, *ACS Appl. Mater. Interfaces* **2021**, *13*, 56358.
[112] Y. Wang, J. Li, X. Yao, C. Xie, Q. Chen, W. Liu, Z. Gao, Y. Fu, Q. Liu, D. He, Y. Li, *ACS Appl. Mater. Interfaces* **2022**, *14*, 40930.
[113] H. W. Qiao, M. Chen, Z. Zhou, Q. Cheng, Y. Hou, H. G. Yang, *Front. Energy Res.* **2021**, *9*, 692059.
[114] A. A. Khan, M. Azam, D. Eric, G. Liang, Z. Yu, *J. Mater. Chem. C* **2020**, *8*, 2880.
[115] R. Li, J. Peng, Y. Xu, W. Li, L. Cui, Y. Li, Q. Lin, *Adv. Opt. Mater.* **2020**, *9*, 2001587.
[116] D. Zheng, T. Zhu, Y. Yan, T. Pauporté, *Adv. Energy Mater.* **2022**, *12*, 2103618.
[117] D. Zheng, C. Schwob, Y. Prado, Z. Ouzit, L. Coolen, T. Pauporté, *Nano Energy* **2022**, *94*, 106934.
[118] D. Zheng, F. Raffin, P. Volovitch, T. Pauporté, *Nat. Commun.* **2022**, *13*, 6655.
[119] D. Zheng, T. Zhu, T. Pauporté, *Sol. RRL* **2021**, 2100010.
[120] D. Zheng, T. Pauporté, *J. Mater. Chem. A* **2021**, *9*, 17801.
[121] F. Zheng, C. Zuo, M. Niu, C. Zhou, S. J. Bradley, C. R. Hall, W. Xu, X. Wen, X. Hao, M. Gao, T. A. Smith, K. P. Ghiggino, *ACS Appl. Mater. Interfaces* **2020**, *12*, 25980.
[122] Z. Li, N. Liu, K. Meng, Z. Liu, Y. Hu, Q. Xu, X. Wang, S. Li, L. Cheng, G. Chen, *Nano Lett.* **2019**, *19*, 5237.
[123] H. Xu, Y. Jiang, T. He, S. Li, H. Wang, Y. Chen, M. Yuan, J. Chen, *Adv. Funct. Mater.* **2019**, *29*, 1807696.
[124] H. Chen, Y. Xia, B. Wu, F. Liu, T. Niu, L. Chao, G. Xing, T. Sum, Y. Chen, W. Huang, *Nano Energy* **2019**, *56*, 373.
[125] F. Huang, P. Siffalovic, B. Li, S. Yang, L. Zhang, P. Nadazdy, G. Cao, J. Tian, *Chem. Eng. J.* **2020**, *394*, 124959.
[126] X. Zhang, G. Wu, W. Fu, M. Qin, W. Yang, J. Yan, Z. Zhang, X. Lu, H. Chen, *Adv. Energy Mater.* **2018**, *8*, 1702498.
[127] W. Fu, J. Wang, L. Zuo, K. Gao, F. Liu, D. S. Ginger, A. K.-Y. Jen, *ACS Energy Lett.* **2018**, *3*, 2086.
[128] K.-R. Yun, T.-J. Lee, S.-K. Kim, J.-H. Kim, T.-Y. Seong, *Adv. Opt. Mater.* **2022**, *11*, 2201974.

[129] X. Chen, Y. Xia, Q. Huang, Z. Li, A. Mei, Y. Hu, T. Wang, R. Cheacharoen, Y. Rong, H. Han, *Adv. Energy Mater.* **2021**, *11*, 2100292.
[130] J. Qing, X.-K. Liu, M. Li, F. Liu, Z. Yuan, E. Tiukalova, Z. Yan, M. Duchamp, S. Chen, Y. Wang, S. Bai, J.-M. Liu, H. J. Snaith, C.-S. Lee, T. C. Sum, F. Gao, *Adv. Energy Mater.* **2018**, *8*, 1800185.
[131] Z. Li, Y. Liu, J. He, G. Yan, G. Cen, B. Jiang, C. Zhao, Y. Yuan, W. Mai, *Surf. Interfaces* **2022**, *29*, 101705.
[132] T. Kim, S. Jeong, K.-H. Kim, H. Shim, D. Kim, H.-J. Kim, *ACS Appl. Mater. Interfaces* **2022**, *14*, 26004.
[133] M. Abdi-Jalebi, Z. Andaji-Garmaroudi, S. Cacovich, C. Stavrakas, B. Philippe, J. M. Richter, M. Alsari, E. P. Booker, E. M. Hutter, A. J. Pearson, S. Lilliu, T. J. Savenije, H. Rensmo, G. Divitini, C. Ducati, R. H. Friend, S. D. Stranks, *Nature* **2018**, *555*, 497.
[134] A. Abate, M. Saliba, D. J. Hollman, S. D. Stranks, K. Wojciechowski, R. Avolio, G. Grancini, A. Petrozza, H. J. Snaith, *Nano Lett.* **2014**, *14*, 3247.
[135] Q. Wang, Q. Dong, T. Li, A. Gruverman, J. Huang, *Adv. Mater.* **2016**, *28*, 6734.
[136] J. Li, H. Li, L. Liu, H. Yao, B. Tian, C. Su, H. Zhong, Y. Wang, L. Zhang, Y. Shi, *Chem. Asian J.* **2019**, *14*, 2861.
[137] J. Li, Z. Gao, X. Hu, S. Wang, Y. Liu, C. Wang, K. Dong, Z. Zeng, C. Tao, G. Fang, *Adv. Funct. Mater.* **2022**, *33*, 2211657.
[138] D. Luo, W. Yang, Z. Wang, A. Sadhanala, Q. Hu, R. Su, R. Shivanna, G. F. Trindade, J. F. Watts, Z. Xu, T. Liu, K. Chen, F. Ye, P. Wu, L. Zhao, J. Wu, Y. Tu, Y. Zhang, X. Yang, W. Zhang, R. H. Friend, Q. Gong, H. J. Snaith, R. Zhu, *Science* **2018**, *360*, 1442.
[139] H. Zhao, T. Li, J. Li, Q. Li, S. Wang, C. Zheng, J. Li, M. Li, Y. Zhang, J. Yao, *J. Alloys Compd.* **2022**, *908*, 164482.
[140] T. Du, F. Richheimer, K. Frohna, N. Gasparini, L. Mohan, G. Min, W. Xu, T. J. Macdonald, H. Yuan, S. R. Ratnasingham, S. Haque, F. A. Castro, J. R. Durrant, S. D. Stranks, S. Wood, M. A. Mclachlan, J. Briscoe, *Nano Lett.* **2022**, *22*, 979.
[141] Y. Zhang, J. Chen, X. Lian, M. Qin, J. Li, T. R. Andersen, X. Lu, G. Wu, H. Li, H. Chen, *Small Methods* **2019**, *3*, 1900375.
[142] L. Lin, J. T.-W. Wang, T. W. Jones, M. Grigore, A. Cook, D. W. Dequilettes, R. Brenes, B. C. Duck, K. F. Anderson, N. W. Duffy, B. Wenger, V. Bulovic, J. Pu, J. Li, B. Chi, H. J. Snaith, G. J. Wilson, *J. Mater. Chem. A* **2019**, *7*, 25511.
[143] Z. Xiao, Q. Dong, C. Bi, Y. Shao, Y. Yuan, J. Huang, *Adv. Mater.* **2014**, *26*, 6503.
[144] S. Xiao, Y. Bai, X. Meng, T. Zhang, H. Chen, X. Zheng, C. Hu, Y. Qu, S. Yang, *Adv. Funct. Mater.* **2017**, *27*, 1604944.
[145] C. Bao, W. Zhu, J. Yang, F. Li, S. Gu, Y. Wang, T. Yu, J. Zhu, Y. Zhou, Z. Zou, *ACS Appl. Mater. Interfaces* **2016**, *8*, 23868.
[146] H. Deng, X. Yang, D. Dong, B. Li, D. Yang, S. Yuan, K. Qiao, Y.-B. Cheng, J. Tang, H. Song, *Nano Lett.* **2015**, *15*, 7963.
[147] Y. Fang, J. Huang, *Adv. Mater.* **2015**, *27*, 2804.
[148] B. Du, W. Yang, Q. Jiang, H. Shan, D. Luo, B. Li, W. Tang, F. Lin, Bo Shen, Q. Gong, X. Zhu, R. Zhu, Z. Fang, *Adv. Opt. Mater.* **2018**, *6*, 1701271.
[149] S. Tong, J. Sun, C. Wang, Y. Huang, C. Zhang, J. Shen, H. Xie, D. Niu, S. Xiao, Y. Yuan, J. He, J. Yang, Y. Gao, *Adv. Electron. Mater.* **2017**, *3*, 1700058.
[150] Y. Zhao, C. Li, J. Jiang, B. Wang, L. Shen, *Small* **2020**, *16*, 2001534.
[151] Y. Wang, X. Liu, L. Li, C. Ji, Z. Sun, S. Han, K. Tao, J. Luo, *Chem. Asian J.* **2019**, *14*, 1530.
[152] C. Fang, H. Wang, Z. Shen, H. Shen, S. Wang, J. Ma, J. Wang, H. Luo, D. Li, *ACS Appl. Mater. Interfaces* **2019**, *11*, 8419.

Daming Zheng received his Ph.D. from Chimie ParisTech, PSL Research University in 2021. During his Ph.D., he was the first researcher to develop the application of in situ/real-time glow discharge optical emission spectroscopy (GD-OES) detection technology in the field of photovoltaic materials worldwide. He is now a post-doctoral researcher at PSL Research College. His main research activities focus on the development of new optoelectronic materials and their application to solar cells and photodetectors.

Thierry Pauporté is a director of research at the Centre National de la Recherche Scientifique (CNRS) in France and he works at Chimie-Paristech, PSL University. He graduated in chemistry from the École Normale Supérieure de Lyon (ENS-L) in France. He received his Ph.D. in physical chemistry from Montpellier II University, France, in 1995. His research interests include oxide and perovskite semiconductors, the functionalizing of the materials surfaces, and he works on the integration of films and structures in efficient devices. The applications studied include light emitting diodes, perovskite solar cells, dye-sensitized solar cells, nanosensors, photodetectors, photocatalysis, wettability, and fouling.